Vibration Control

ADVANCED COURSE ON STRUCTURAL CONTROL AND HEALTH MONITORING
SMART'01 – (PP.13–53) – WARSAW, MAY 22-25, 2001.

Active vibration control

A. PREUMONT

Université Libre de Bruxelles
Brussels, Belgium

This paper consists of an introduction to smart structures and their applications in the area of vibration control. The first part addresses important issues in the modelling of smart piezoelectric structures. It is followed by a review of control strategies for active damping using collocated actuator/sensor configurations, including the active tendon control of cable structures and a generic active damping interface based on a Stewart platform. Finally, the active vibration isolation is addressed for a single axis and six degrees of freedom

1. Introduction

In order to motivate the use of active vibration control, consider the future interferometric missions planned by NASA or ESA (one such a mission, called "Terrestrial Planet Finder" aims at detecting earth-sized planets outside the solar system; other missions include the mapping of the sky with an accuracy one order better than that achieved by *Hypparcos*).

The purpose is to use a number of smaller telescopes as an interferometer to achieve a resolution which could only be achieved with a much larger monolythic telescope. One possible spacecraft architecture for such an interferometric mission is represented in Fig. 1; it consists of a main truss supporting a set of independently pointing telescopes.

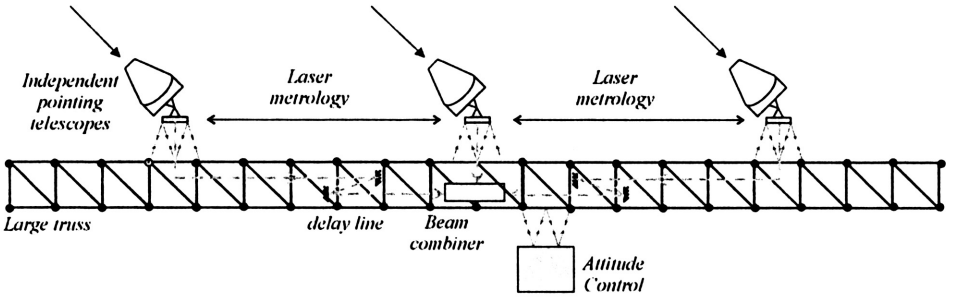

FIGURE 1. Schematic view of a future interferometric mission.

The relative position of the telescopes is monitored by a sophisticated metrology and the optical paths between the individual telescopes and the beam combiner are accurately controlled with optical delay lines, based on the information coming from a wave

front sensor. Typically, the distance between the telescopes could be 50 m or more, and the order of magnitude of the error allowed on the optical path length is a few nanometers; the pointing error of the individual telescopes is as low as a few nanoradians (i.e. one order of magnitude better than the Hubble space telescope). Clearly, such stringent geometrical requirements cannot be achieved with a precision monolithic structure, but rather by active means as suggested in Fig. 1. Let us first consider the supporting truss: given its size and environment, the main requirement on the supporting truss is not *precision* but *stability*, the accuracy of the optical path being taken care of by the wide-band vibration isolation/steering control system of individual telescopes and the optical delay lines (described below). Geometric stability includes thermal stability, vibration damping and prestressing the gaps in deployable structures (this is a critical issue for deployable trusses). In addition to the geometric requirements mentioned above, this spacecraft would be sent in deep space (perhaps as far as the orbit of Jupiter) to ensure maximum sensitivity; this makes the weight issue particularly important.

Another interesting subsystem necessary to achieve the stringent specifications is the six d.o.f. vibration isolator at the interface between the attitude control module and the supporting truss; this isolator allows the low frequency attitude control torque to be transmitted while filtering out the high frequency disturbances generated by the unbalanced centrifugal forces in the reaction wheels. The same general purpose vibration isolator may be used at the interface between the truss and the independent telescopes; in this case however, its vibration isolation capability is combined with the steering (pointing) of the telescopes. The third component relevant of active control is the optical delay line; it consists of a high precision single degree of freedom translational mechanism supporting a mirror, whose function is to control the path length between every telescope and the beam combiner, so that these distances are kept identical to a fraction of the wavelength (e.g. $\lambda/20$).

Performance and weight savings are the prime motivations of the foregoing example. However, as technology develops and with the availability of low cost electronic components, it is likely that there will be a growing number of applications where active solutions will become cheaper than passive ones, for the same level of performance.

The reader should not conclude that *active* will always be better and that a control system can compensate for a bad design. In most cases, a bad design will remain bad, active or not, and an active solution should normally be considered only after all other passive means have been exhausted. One should always bear in mind that feedback control can compensate external disturbances only in a limited frequency band that is called the *bandwidth* of the control system. One should never forget that outside the bandwidth, the disturbance is actually amplified by the control system.

In recent years, there has been a growing interest for *semi-active* control, particularly for vehicle suspensions; this has been driven by the reduced cost as compared to active control, due mainly to the absence of a large power actuator. A semi-active device can be broadly defined as a passive device in which the properties (stiffness, damping, ...) can be varied in real time with a low power input. Although they behave in a strongly nonlinear way, semi-active devices are inherently passive and, unlike active devices, cannot destabilize the system; they are also less vulnerable to power failure. Semi-active suspension devices may be based on classical viscous dampers with a variable orifice, or on magneto-rheological (MR) fluids.

2. Smart materials and structures

An active structure consists of a structure provided with a set of actuators and sensors coupled by a controller; if the bandwidth of the controller includes some vibration modes of the structure, its dynamic response must be considered. If the set of actuators and sensors are located at discrete points of the structure, they can be treated separately. The distinctive feature of *smart* structures is that the actuators and sensors are often distributed and have a high degree of integration inside the structure, which makes a separate modelling impossible (Fig. 2). Moreover, in some applications like vibroacoustics, the behaviour of the structure itself is highly coupled with the surrounding medium; this also requires a coupled modelling.

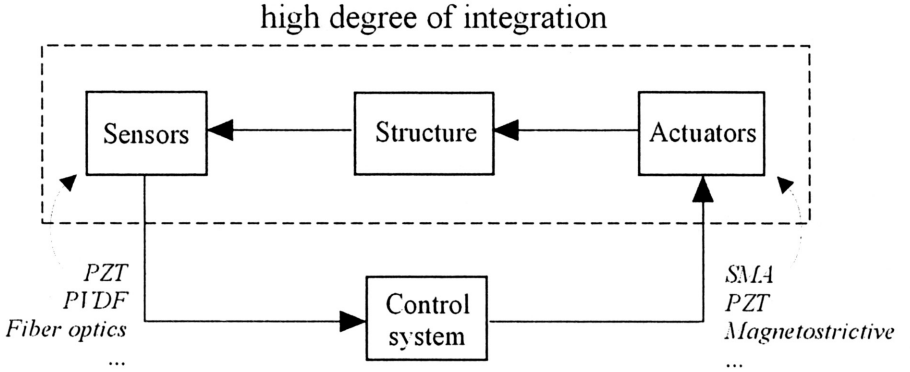

FIGURE 2. Smart structure.

From a mechanical point of view, classical structural materials are entirely described by their elastic constants relating stress and strain, and their thermal expansion coefficient relating the strain to the temperature. *Smart materials* are materials where strain can also be generated by different mechanisms involving temperature, electric field or magnetic field, etc... as a result of some coupling in their constitutive equations. The most celebrated smart materials are briefly described below:

- *Shape Memory Alloys (SMA)* allow one to recover up to 5% strain from the phase change induced by temperature. Although two-way applications are possible after education, *SMA*s are best suited for one-way tasks such as deployment. In any case, they can be used only at low frequency and for low precision applications, mainly because of the difficulty of cooling. Fatigue under thermal cycling is also a problem. The best known *SMA* is the *NITINOL*; *SMA*s are little used in vibration control and will not be discussed in this book.
- *Piezoelectric materials* have a recoverable strain of 0.1% under electric field; they can be used as actuators as well as sensors. There are two broad classes of piezoelectric materials used in vibration control: ceramics and polymers. The piezopolymers are used mostly as sensors, because they require extremely high voltages and they have a limited control authority; the best known is the *polyvinylidene fluoride* ($PVDF$ or PVF_2). Piezoceramics are used extensively as actuators and sensors, for a wide range of frequency including ultrasonic applications; they are

well suited for high precision in the nanometer range ($1\,\text{nm} = 10^{-9}\,\text{m}$). The best known piezoceramic is the *Lead Zirconate Titanate (PZT).*

- *Magnetostrictive materials* have a recoverable strain of 0.15% under magnetic field; the maximum response is obtained when the material is subjected to compressive loads. Magnetostrictive actuators can be used as load carrying elements (in compression alone) and they have a long lifetime. They can also be used in high precision applications. The best known is the *TERFENOL-D.*
- *Magneto-rheological (MR)* fluids consists of viscous fluids containing micron-sized particles of magnetic material. When the fluid is subjected to a magnetic field, the particles create columnar structures requiring a minimum shear stress to initiate the flow. This effect is reversible and very fast (response time of the order of millisecond). Some fluids exhibit the same behaviour under electrical field; they are called *electro-rheological (ER)* fluids; however, their performances (limited by the electric field breakdown) are significantly inferior to *MR* fluids. *MR* and *ER* fluids are used in semi-active devices.

This brief list of commercially available smart materials is just a flavor of what is to come: *phase change materials* are currently under development and are likely to become available in a few years time; they will offer a recoverable strain of the order of 1% under an electric field, one order of magnitude more than the piezoceramics.

The range of available devices to measure position, velocity, acceleration and strain is extremely wide, and there are more to come, particularly in optomechanics. Displacements can be measured with inductive, capacitive and optical means (laser interferometer); the latter two have a resolution in the nanometer range. Piezoelectric accelerometers are very popular but they cannot measure a d.c. component. Strain can be measured with strain gages, piezoceramics, piezopolymers and fiber optics. The latter can be embedded in a structure and give a global average measure of the deformation; they offer a great potential for health monitoring as well. We will see that piezopolymers can be shaped to react only to a limited set of vibration modes (modal filters).

3. Control strategies

There are two radically different approaches to disturbance rejection: feedback and feedforward. Although this text is entirely devoted to feedback control, it is important to point out the salient features of both approaches, in order to enable the user to select the most appropriate one for a given application.

3.1. Feedback

The principle of feedback is represented in Fig. 3; the output y of the system is compared to the reference input r and the error signal, $e = r - y$, is passed into a compensator $H(s)$ and applied to the system $G(s)$. The design problem consists of finding the appropriate compensator $H(s)$ such that the closed-loop system is stable and behaves in the appropriate manner.

In the control of lightly damped structures, feedback control is used for two distinct and somewhat complementary purposes: *active damping* and *model based* feedback.

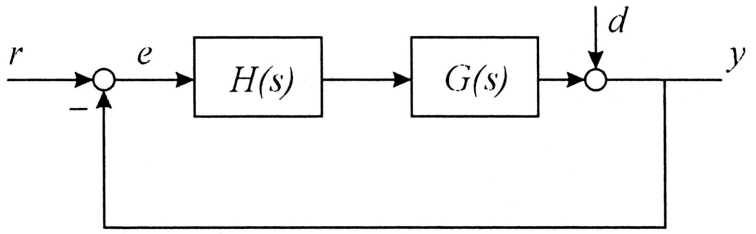

FIGURE 3. Principle of feedback control.

The objective of active damping is to reduce the resonant peaks of the closed-loop transfer function

$$F(s) = \frac{y(s)}{r(s)} = \frac{GH}{1+GH}. \tag{1}$$

In this case $F(s)$ is very close to $G(s)$, except near the resonance peaks where the amplitude is reduced. Active damping can generally be achieved with moderate gains; another nice property is that it can be achieved without a model of the structure and with guaranteed stability, provided that the actuator and sensor are collocated and have perfect dynamics. Of course actuators and sensors always have finite dynamics and any active damping system has a finite bandwidth.

The control objectives can be more ambitious and we may wish to keep a control variable (a position, or the pointing of an antenna) to a desired value in spite of external disturbances d in some frequency range. From

$$\frac{y(s)}{d(s)} = \frac{1}{1+GH} \tag{2}$$

we readily see that reducing the effect of external disturbances requires large values of GH in the frequency range where the disturbance is significant. From Eq. (1), we see that $GH \gg 1$ implies that the closed-loop transfer function $F(s)$ is close to 1, which means that the output y tracks the input r accurately. In general, to achieve that, we need a more elaborate strategy involving a mathematical model of the system which, at best, can only be a low-dimensional approximation of the actual system $G(s)$. There are many techniques available to find the appropriate compensator and only the simplest and the best established will be reviewed in this text. They all have a number of common features:

- The bandwidth ω_c of the control system is limited by the accuracy of the model; there is always some destabilization of the flexible modes outside ω_c (residual modes). The phenomenon whereby the net damping of the residual modes actually decreases when the bandwidth increases is known as *spillover* (Fig. 4).
- The disturbance rejection within the bandwidth of the control system is always compensated by an amplification of the disturbances outside the bandwidth.
- When implemented digitally, the sampling frequency ω_s must always be two orders of magnitude larger than ω_c to preserve reasonably the behaviour of the continuous system. This puts some hardware restrictions on the bandwidth of the control system.

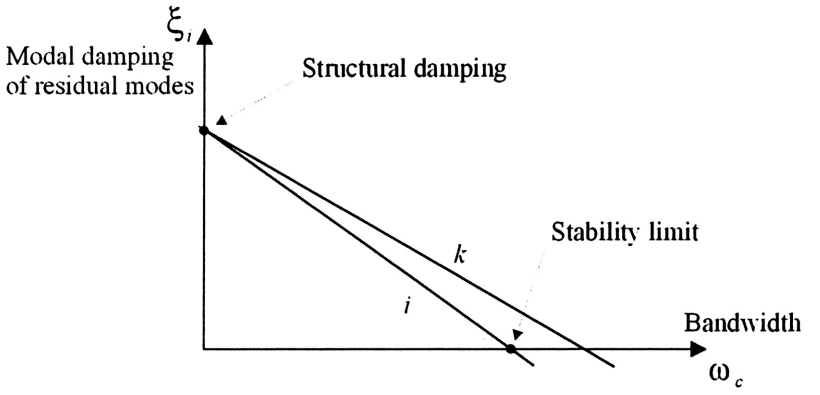

FIGURE 4. Effect of the control bandwidth on the net damping of the residual modes.

3.2. Feedforward

When a signal correlated to the disturbance is available, feedforward adaptive filtering constitutes an attractive alternative to feedback for disturbance rejection; it was originally developed for noise control [21], but it is very efficient for vibration control too [12]. Its principle is explained in Fig. 5. The method relies on the availability of a reference signal correlated to the primary disturbance; this signal is passed through an adaptive filter, the output of which is applied to the system by secondary sources. The filter coefficients are adapted in such a way that the error signal at one or several critical points is minimized. The idea is to produce a secondary disturbance such that it cancels the effect of the primary disturbance at the location of the error sensor. Of course, there is no guarantee that the global response is also reduced at other locations and, unless the response is dominated by a single mode, there are places where the response can be amplified; the method can therefore be considered as a local one, in contrast to feedback which is global. Unlike active damping which can only attenuate the disturbances

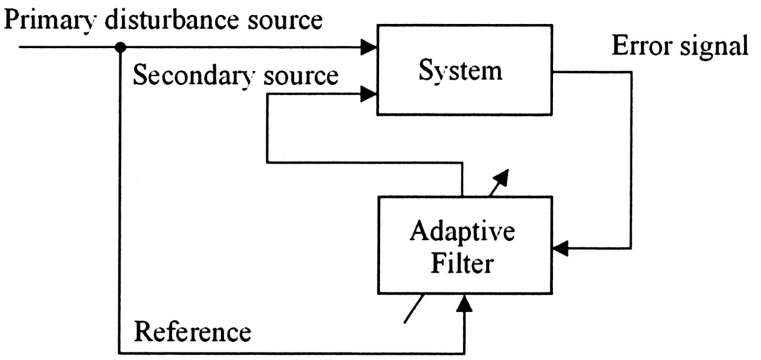

FIGURE 5. Principle of feedforward control.

near the resonances, feedforward works for any frequency and attempts to cancel the disturbance completely by generating a secondary signal of opposite phase.

The method does not need a model of the system, but the adaption procedure relies on the measured impulse response. The approach works better for narrow-band disturbances, but wide-band applications have also been reported. Because it is less sensitive to phase lag than feedback, feedforward control can be used at higher frequency (a good rule of thumb is $\omega_c \simeq \omega_s/10$); this is why it has been so successful in acoustics.

The main limitation of feedforward adaptive filtering is the availability of a reference signal correlated to the disturbance. There are many applications where such a signal can be readily available from a sensor located on the propagation path of the perturbation. For disturbances induced by rotating machinery, an impulse train generated by the rotation of the main shaft can be used as reference. Table 1 summarizes the main features of the two approaches.

TABLE 1. Comparison of control strategies.

Type of control	Advantages	Disadvantages
Feedback		
Active damping	• no model needed • guaranteed stability when collocated	• effective only near resonances
Model based (LQG, $H_\infty \ldots$)	• global method • attenuates all disturbances within ω_c	• limited bandwidth ($\omega_c \ll \omega_s$) • disturbances outside ω_c are amplified • spillover
Feedforward		
Adaptive filtering of reference (*x-filtered LMS*)	• no model necessary • wider bandwidth ($\omega_c \simeq \omega_s/10$) • works better for narrow-band disturb.	• reference needed • local method (response may be amplified in some part of the system) • large amount of real time computations

4. Open-loop frequency response

Consider a lightly damped flexible structure provided with a point force actuator and a displacement sensor. The open-loop frequency response function (FRF) can be expanded in modal coordinates as

$$G(\omega) = \sum_{i=1}^{n} \frac{\phi_i(a)\phi_i(s)}{\mu_i(\omega_i^2 - \omega^2 + 2j\xi_i\omega_i\omega)}, \tag{3}$$

where ω_i is the natural frequency of mode i, μ_i its modal mass, ξ_i its modal damping, and $\phi_i(a)$ and $\phi_i(s)$ are the modal amplitudes at the actuator and sensor locations, respectively; in principle, the sum extends to all the modes of the structure. If one wish to truncate the modal expansion above the frequency range of interest, it is very important to keep the static contribution of the high frequency modes:

$$G(\omega) \simeq \sum_{i=1}^{m} \frac{\phi_i(a)\phi_i(s)}{\mu_i(\omega_i^2 - \omega^2 + 2j\xi_i\omega_i\omega)} + \sum_{i=m+1}^{n} \frac{\phi_i(a)\phi_i(s)}{\mu_i\omega_i^2}. \tag{4}$$

The second sum is often called *residual mode*; it is independent of ω and introduces a *feedthrough* component in the FRF. It can be shown that this term plays an important role in the location of the open-loop zeros of the system. Upon writing Eq. (4) for $\omega = 0$, it is readily obtained that the residual mode can be written alternatively

$$R = \sum_{i=m+1}^{n} \frac{\phi_i(a)\phi_i(s)}{\mu_i\omega_i^2} = G(0) - \sum_{i=1}^{m} \frac{\phi_i(a)\phi_i(s)}{\mu_i\omega_i^2}. \tag{5}$$

4.1. Collocated systems

Consider an undamped system with collocated actuator and sensor. Since $\phi_i(a) = \phi_i(s)$, Eq. (4) becomes

$$G(\omega) \simeq \sum_{i=1}^{m} \frac{\phi_i^2(a)}{\mu_i(\omega_i^2 - \omega^2)} + R. \tag{6}$$

We note that the residues are all positive.

The behaviour of $G(\omega)$ is represented in Fig. 6; the amplitude of $G(\omega)$ goes to $\pm\infty$ at the resonance frequencies ω_i (corresponding to a pair of imaginary poles in the system). Besides, as $G(\omega)$ is an increasing function of ω^2, in every interval between consecutive resonance frequencies, there is a frequency ω_{0i} where the amplitude of the FRF vanishes; these frequencies are known in structural dynamics as *anti-resonance*; they correspond to purely imaginary zeros. Thus an undamped structure with collocated actuator and sensor has *alternating poles and zeros on the imaginary axis* (Fig. 7a).

The transfer function can be written alternatively

$$G(s) = k\frac{\prod_{\text{zeros}}(s^2 + \omega_{0i}^2)}{\prod_{\text{poles}}(s^2 + \omega_i^2)}. \tag{7}$$

If some damping is added, the poles and zeros are slightly moved into the left half plane as indicated in Fig. 7b, without changing the dominant feature of interlacing.

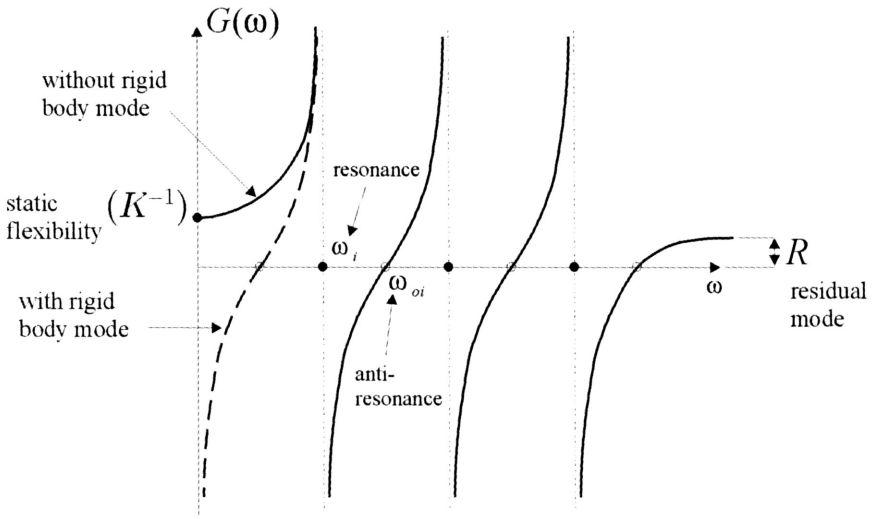

FIGURE 6. FRF of an undamped structure with collocated actuator and sensor.

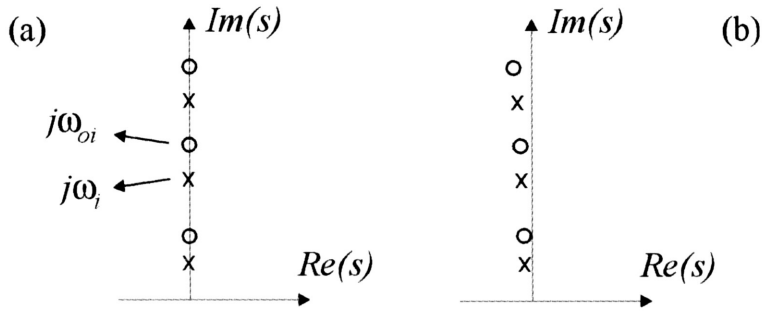

FIGURE 7. Pole/zero pattern of a structure with collocated actuator and sensor. (a) Undamped. (b) Lightly damped. (Only the upper half of the complex plane is shown, the diagram is symmetrical with respect to the real axis).

A collocated system always exhibits Bode and Nyquist plots similar to those represented in Fig. 8. Each flexible mode introduces a circle in the Nyquist diagram; it is more or less centered on the imaginary axis which is intersected at $\omega = \omega_i$ and $\omega = \omega_{0i}$; the radius of each circle is proportional to the inverse of the modal damping, ξ_i^{-1}. In the Bode plots, a 180° phase lag occurs at every natural frequency, and is compensated by a 180° phase lead at every imaginary zero; the phase always oscillates between 0 and $-\pi$, as a result of the interlacing property of the poles and zeros. It is worth pointing out that the zeros (anti-resonance) of a collocated system are identical to the resonance frequencies of the system with an additional restraint at the actuator/sensor location.

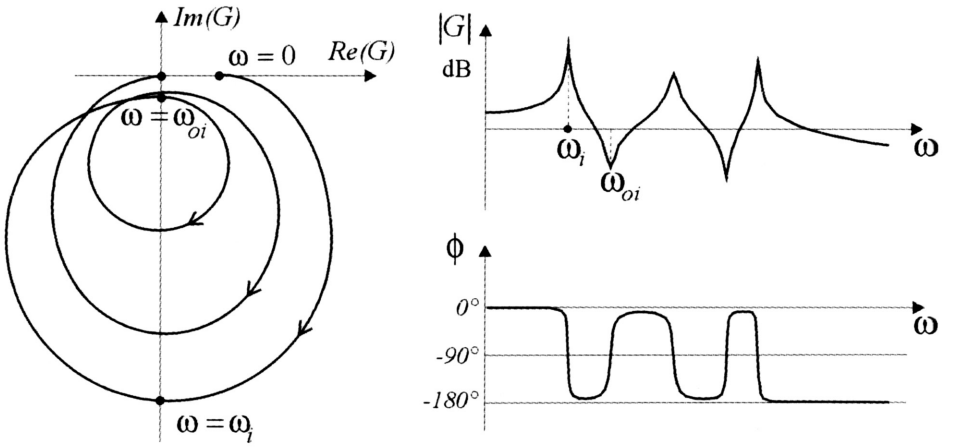

FIGURE 8. Nyquist diagram and Bode plots of a lightly damped structure with collocated actuator and sensor.

5. Laminar piezoelectric actuator

5.1. Smart piezoelectric shell

Consider a two-dimensional piezoelectric lamina in a plane (x, y); the poling direction is z (normal to the lamina) and the electric field is also applied along z. In the piezoelectric principal axes, the constitutive equations read

$$\{T\} = [C]\{S\} - \begin{Bmatrix} e_{31} \\ e_{32} \\ 0 \end{Bmatrix} E, \tag{8}$$

$$D = \{e_{31} \quad e_{32} \quad 0\}\{S\} + \varepsilon E, \tag{9}$$

where

$$\{T\} = \begin{Bmatrix} \sigma_x \\ \sigma_y \\ \sigma_{xy} \end{Bmatrix}, \qquad \{S\} = \begin{Bmatrix} \varepsilon_x = \dfrac{\partial u}{\partial x} \\ \varepsilon_y = \dfrac{\partial v}{\partial y} \\ \gamma_{xy} = \dfrac{\partial u}{\partial y} + \dfrac{\partial v}{\partial x} \end{Bmatrix} \tag{10}$$

are the stress and strain vector, respectively, $[C]$ is the matrix of elastic constant, E is the component of the electric field along z, D is the z-component of the electric displacement and ε the dielectric constant and e_{31} and e_{32} are the piezoelectric constants.

Next, consider a piezoelectric lamina bounded on a shell structure (Fig. 9). If the global axes coincide with the piezoelectric axes of the lamina, the constitutive equations can be integrated over the thickness of the shell in the form (e.g. [17])

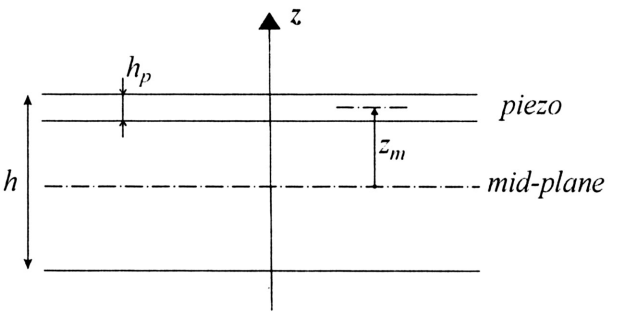

FIGURE 9. Piezoelectric shell.

$$\begin{Bmatrix} N \\ M \end{Bmatrix} = \begin{bmatrix} A & B \\ B & D \end{bmatrix} \begin{Bmatrix} S_0 \\ \kappa \end{Bmatrix} + \begin{bmatrix} I_3 \\ z_m I_3 \end{bmatrix} \begin{Bmatrix} e_{31} \\ e_{32} \\ 0 \end{Bmatrix} V, \tag{11}$$

$$D = \{e_{31} \quad e_{32} \quad 0\} \begin{bmatrix} I_3 & z_m I_3 \end{bmatrix} \begin{Bmatrix} S_0 \\ \kappa \end{Bmatrix} - \frac{\varepsilon}{h_p} V, \tag{12}$$

where $\{N\}$ is the vector of in-plane resultant forces and $\{M\}$ the vector of bending moments:

$$\{N\} = \int_{-h/2}^{h/2} \{T\}\, dz, \qquad \{M\} = \int_{-h/2}^{h/2} \{T\}\, z\, dz. \tag{13}$$

$\{S_0\}$ is the deformation vector of the mid-plane and $\{\kappa\}$ is the vector of curvatures:

$$\{S_0\} = \begin{Bmatrix} \dfrac{\partial u_0}{\partial x} \\ \dfrac{\partial v_0}{\partial y} \\ \dfrac{\partial u_0}{\partial y} + \dfrac{\partial v_0}{\partial x} \end{Bmatrix}, \qquad \{\kappa\} = \begin{Bmatrix} \dfrac{\partial^2 w}{\partial x^2} \\ \dfrac{\partial^2 w}{\partial y^2} \\ \dfrac{\partial^2 w}{\partial x \partial y} \end{Bmatrix}. \tag{14}$$

The matrices A, B, D are the classical stiffness matrices of the shell theory (e.g. [3]); h_p is the thickness of the piezoelectric lamina and z_m is the distance between its mid-plane and the mid-plane of the shell.

If the piezoelectric lamina is connected to a charge amplifier, the voltage between the electrodes is set to $V = 0$ and the sensor equation (12) can be integrated over the electrode to produce the sensor output

$$Q = \int_{\Omega} \left[e_{31} \frac{\partial u_0}{\partial x} + e_{32} \frac{\partial v_0}{\partial y} + z_m \left(e_{31} \frac{\partial^2 w}{\partial x^2} + e_{32} \frac{\partial^2 w}{\partial y^2} \right) \right] dS, \tag{15}$$

where the integral extends over the surface of the electrode (the part of the piezo not covered by the electrode does not contribute to the signal). The first part of the integral

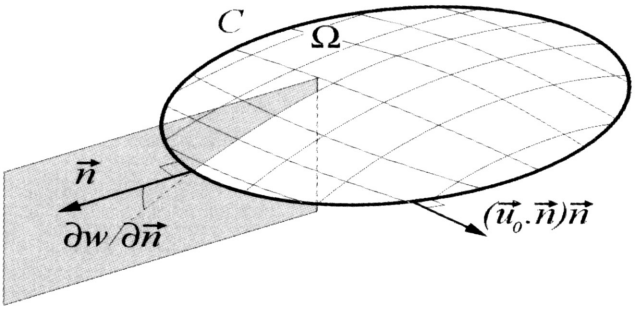

$$Q = e_{31} \int_C \left(\underbrace{\vec{u}_0.\vec{n}}_{\substack{\text{displacement} \\ \text{normal to} \\ \text{the contour}}} + z_m \underbrace{\frac{\partial w}{\partial \vec{n}}}_{\text{slope}} \right) dl$$

FIGURE 10. Sensor equation for an isotropic piezo.

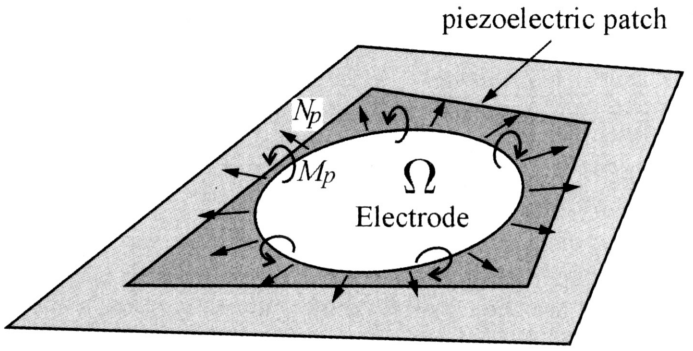

$$\underbrace{N_p = -e_{31} V}_{\text{normal force}} \qquad \underbrace{M_p = -e_{31} z_m V}_{\text{bending moment}}$$

FIGURE 11. Equivalent piezoelectric forces for an isotropic piezo.

is the contribution of the membrane strain while the second one is due to bending. If the piezoelectric properties are isotropic ($e_{31} = e_{32}$), the surface integral can be further transformed into a contour integral using one of the Green integrals:

$$Q = e_{31} \int_C \left(\vec{u_0} \cdot .\vec{n} + z_m \frac{\partial w}{\partial \vec{n}} \right) dl. \tag{16}$$

This integral extends over the contour of the electrode (Fig. 10); the first contribution is the component of the mid-plane in-plane displacement normal to the contour and the second one is associated with the slope along the contour.

Similarly, for a piezoelectric actuator made of isotropic material, the equivalent piezoelectric loads consist of a in-plane force, normal to the contour of the electrode, and a constant moment, acting along the contour of the electrode (Fig. 11):

$$N_p = -e_{31} V, \qquad M_p = -e_{31} z_m V. \tag{17}$$

5.2. Smart piezoelectric beam

Figure 12 considers the particular case where the piezo patch is mounted on a beam. Of all the piezoelectric forces defined by Eq. (17) and represented in Fig. 12b, only the bending moment M_p normal to the beam axis will contribute significantly to the transverse displacements of the beam (Fig. 12a); this is the corresponding equivalent load of the beam theory.

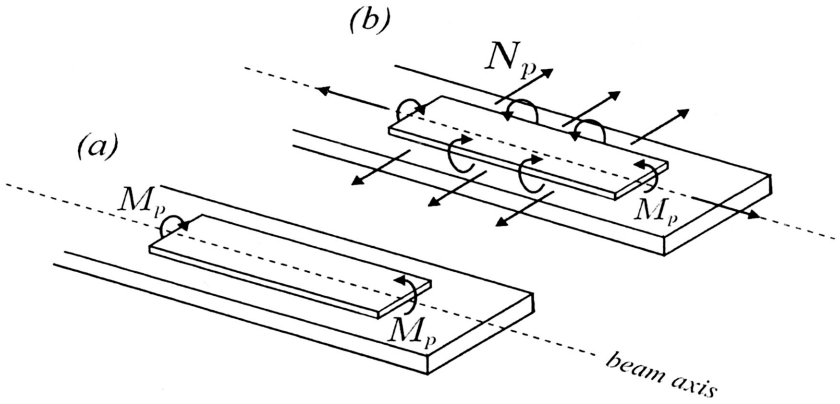

FIGURE 12. Equivalent piezoelectric loads of a rectangular piezoceramic patch on a beam. (a) Beam theory. (b) Shell theory.

In a more general configuration where a beam is covered with a piezoelectric layer with an electrode of width $b_p(x)$, the equivalent piezoelectric load consists of a distributed load proportional to the second derivative of the width of the electrode (e.g. [23]):

$$p = -e_{31} z_m V \, b_p''(x). \tag{18}$$

Similarly, if the piezo layer is used as a sensor, the amount of electric charge generated by the beam deformation is given by

$$Q = -e_{31} z_m \int_a^b \frac{\partial^2 w}{\partial x^2} b_p(x)\, dx, \tag{19}$$

where a and b are the limit of the electrode along the beam. Eq. (19) is a particular case of Eq. (15), with the assumptions of the beam theory.

5.3. Spatial modal filters

Equation (18) allows to tailor an actuator to produce a single mode excitation [18]. Indeed, it can be shown that the electrode profile

$$b_p''(x) \sim m\, \phi_l(x) \tag{20}$$

(where m is the mass per unit length) excites only mode l; this is a consequence of the orthogonality condition of the mode shapes.

Conversely, a sensor with an electrode profile

$$b_p(x) \sim EI\, \phi_l''(x) \tag{21}$$

will be sensitive only to mode l. Note that for an uniform beam, the modal actuator and the modal sensor have the same shape, because $\phi_i^{IV}(x) \sim \phi_i(x)$. Figure 13 illustrates the modal filters used for a uniform beam with various boundary conditions; the change of sign indicates a change in the polarity of the strip, which is equivalent to negative values of $b_p(x)$. As an alternative, the part of the sensor with negative polarity can be bonded on the opposite side of the beam. The reader will notice that the electrode shape of the simply supported beam is the same as the mode shape, while for the cantilever beam, the electrode shape is that of the mode shape of a beam supported at the opposite end.

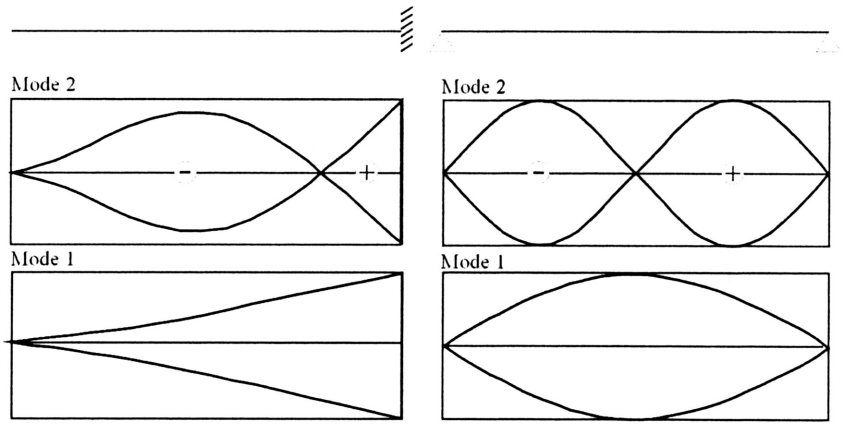

FIGURE 13. Modal filters for the first two modes of a beam for various boundary conditions: (a) cantilever; (b) simply supported.

6. Active truss

Consider the active truss of Fig. 14; when a voltage V is applied to an unconstrained linear piezoelectric actuator, it produces an expansion δ.

$$\delta = d_{33} n V = g_a V, \tag{22}$$

where d_{33} is the piezoelectric coefficient, n is the number of piezoelectric ceramic elements in the actuator; g_a is the actuator gain. This equation neglects the hysteresis of the piezoelectric expansion. If the actuator is placed in a truss, its effect on the structure can be represented by equivalent piezoelectric loads acting on the passive structure. As for thermal loads, the pair of self equilibrating piezoelectric loads applied axially to both ends of the active strut (Fig. 14) has a magnitude equal to the product of the stiffness of the active strut, K_a, by the unconstrained piezoelectric expansion δ:

$$p = K_a \delta. \tag{23}$$

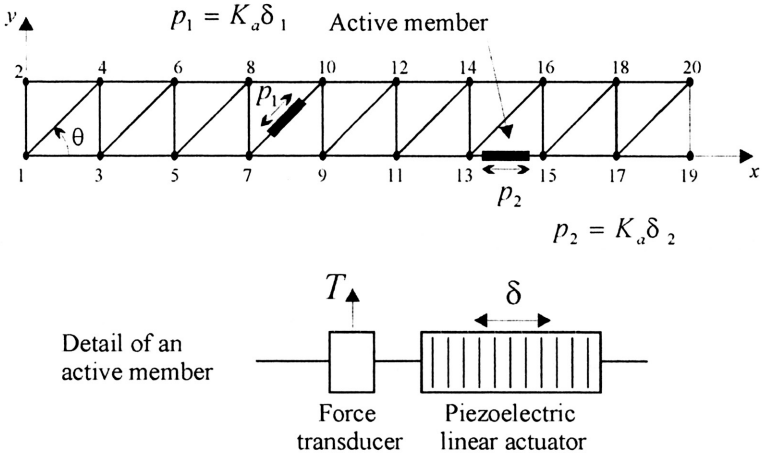

FIGURE 14. Active truss. The active struts consist of a piezoelectric linear actuator colinear with a force transducer.

Assuming no damping, the equation governing the motion of the structure excited by a single actuator is

$$M\ddot{x} + Kx = bp = b K_a \delta, \tag{24}$$

where b is the influence vector of the active strut in the global coordinate system. The non-zero components of b are the direction cosines of the active bar. As for the output signal of the force transducer, it is given by

$$y = T = K_a \delta_e, \tag{25}$$

where δ_e is the elastic extension of the active strut, equal to the difference between the total extension of the strut and its piezoelectric component δ. The total extension

is the projection of the displacements of the end nodes on the active strut, $\Delta = b^T x$. Introducing this into Eq. (25), we get

$$y = T = K_a(b^T x - \delta). \tag{26}$$

Note that, because the sensor is located in the same strut as the actuator, the same influence vector b appears in the sensor equation (26) and the equation of motion (24). If the force sensor is connected to a charge amplifier of gain g_s, the output voltage v_0 is given by

$$v_0 = g_s T = g_s K_a(b^T x - \delta). \tag{27}$$

Note the presence of a feedthrough component from the piezoelectric extension δ. Upon transforming into modal coordinates, the frequency response function (FRF) $G(\omega)$ between the voltage V applied to the piezo and the output voltage of the charge amplifier can be written [23]:

$$\frac{v_0}{V} = G(\omega) = g_s g_a K_a \left\{ \sum_{i=1}^{n} \frac{\nu_i}{1 - \omega^2/\Omega_i^2} - 1 \right\}, \tag{28}$$

where Ω_i are the natural frequencies, and we define

$$\nu_i = \frac{K_a(b^T \phi_i)^2}{\mu_i \Omega_i^2} = \frac{K_a(b^T \phi_i)^2}{\phi_i^T K \phi_i}. \tag{29}$$

The numerator and the denominator of this expression represent respectively twice the strain energy in the active strut and twice the total strain energy when the structure vibrates according to mode i; $\nu_i (\geq 0)$ is therefore called the *modal fraction of strain*

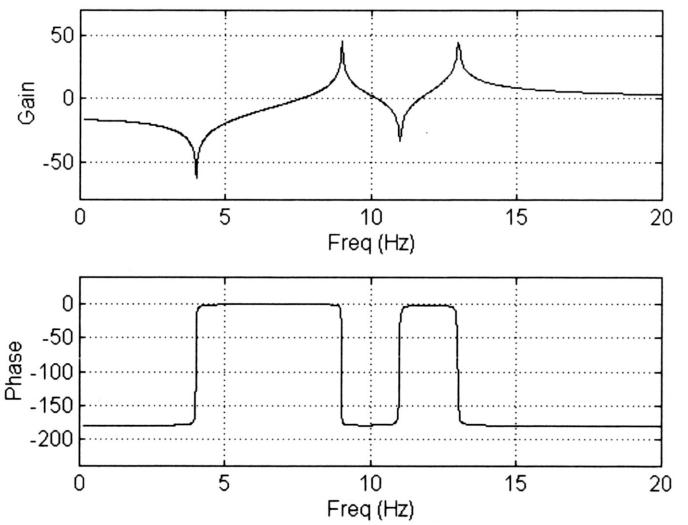

FIGURE 15. Open-loop FRF $G(\omega)$ of the active truss (a small damping is assumed).

energy in the active strut. From Eq. (28), we see that ν_i determines the residue of mode i, that is the amplitude of the contribution of mode i in the transfer function between the piezo actuator and the force sensor; it can therefore be regarded as a compound index of controllability and observability of mode i. ν_i is readily available from commercial finite element programs; it can be used to select the proper location of the active strut in the structure: the best location is that with the highest ν_i for the modes that we wish to control [27]. The FRF (28) has alternating poles and zeros on the imaginary axis (or near, if the structural damping is taken into account) (Fig. 15).

7. Active damping with collocated pairs

7.1. Introduction

The role of damping is to reduce the settling time of the transient response to impulsive loads, and the resonant response to broad band stationary excitations. In this section, we examine various ways of achieving active damping augmentation with collocated actuator/sensor pairs. As we have seen in Sec. 4, this special configuration

TABLE 2. Collocated active damping compensators for various actuator/sensor pairs. The column indicates the type of actuator, and the row the type of sensor.

$gD(s)$	Force	Strain (d_{31} piezo)	Linear (d_{33} piezo)
Displacement	*Lead* $g\frac{s}{s+a}$		
Velocity	*Direct Velocity F.* g		
Acceleration	*DVF*: g/s $\frac{g}{s^2+2\xi_f\omega_f s+\omega_f^2}$		
Strain (d_{31} piezo)		*Positive Position F.* $\frac{-g\omega_f^2}{s^2+2\xi_f\omega_f s+\omega_f^2}$	
Force			*Integral Force F.* $-g/s$

leads to alternating poles and zeros near the imaginary axis; thanks to this property, a number of active damping schemes with guaranteed stability have been developed and tested with various types of actuators and sensors (Table 2); they can be implemented in a decentralized manner, each actuator interacting only with its collocated sensor.

7.2. Direct velocity feedback [5, 6]

Consider an undamped structure controlled with a set of point force actuators u collocated with a set of velocity sensors $\dot{y}$; the governing equations are

structure:

$$M\ddot{x} + Kx = f + Bu, \tag{30}$$

sensor:

$$\dot{y} = B^T \dot{x}, \tag{31}$$

control:

$$u = -G\dot{y}, \tag{32}$$

where B is the control influence matrix and G is the positive definite matrix of control gains. The fact that B^T appears in the sensor equation is due to collocation. Combining the three equations, we find the closed-loop equation

$$M\ddot{x} + BGB^T\dot{x} + Kx = f. \tag{33}$$

Therefore, the control forces appear as a viscous damping (electrodynamic damping). The damping matrix $C = BGB^T$ is positive semi definite, because the actuators and sensors are collocated.

7.2.1. Lead compensator. Let us examine the *SISO* case a little closer. In this case, the matrix B degenerates into a control influence vector B. The open-loop transfer function between the control force u and the collocated displacement y is

$$G_0(s) = \frac{Y(s)}{U(s)} = \sum_i \frac{b^T \phi_i \phi_i^T b}{\mu_i(\omega_i^2 + s^2)}, \tag{34}$$

where the sum extends to all the modes. We know that the corresponding poles and zeros alternate on the imaginary axis.

Because the amplitude of the derivative compensation increases linearly with the frequency, which would lead to noise amplification at high frequency, it is not desirable to implement the compensator as in Eq. (32), but rather to supplement it by a low-pass filter to produce:

$$D(s) = g\frac{s}{s+a}. \tag{35}$$

A pole has been added at some distance a along the negative real axis. This compensator behaves like a derivator at low frequency ($\omega \ll a$). The block diagram of the control system is shown in Fig. 16; a displacement sensor is now assumed and the structural damping is again omitted for simplicity.

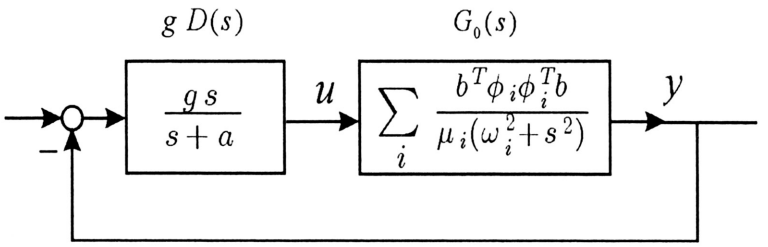

FIGURE 16. Block diagram of the modified direct velocity feedback.

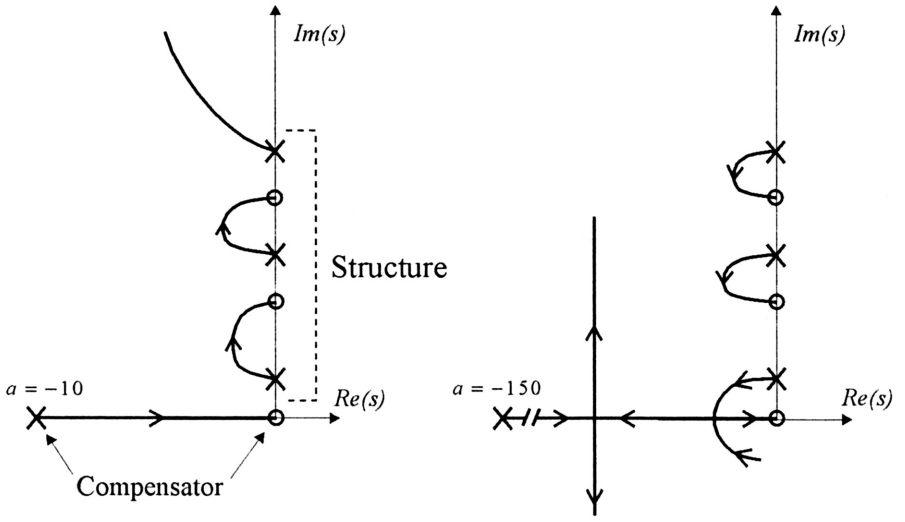

FIGURE 17. Root locus plots for two values of the low-pass filter corner frequency a (only the upper half is shown).

Typical root locus plots are shown in Fig. 17 for two values of the low-pass filter corner frequency a. The closed-loop pole trajectories go from the open-loop poles to the open-loop zeros following branches which are entirely contained in the left half plane. Since there are two poles more than zeros, there are two asymptotes at $\pm 90°$. The system is always stable, and this property is not sensitive to parameter variations, because the alternating pole-zero pattern is preserved under parameter variations.

7.3. Acceleration feedback [28, 29]

The easiest way to use the acceleration is to integrate it to obtain the absolute velocity; the direct velocity feedback can then be used. In practice, however, piezoelectric accelerometers use charge amplifiers which behave as high-pass filters; this does not affect significantly the results if the corner frequency of the charge amplifier is well below the vibration mode of the structure. Next, we consider an alternative controller which also enjoys guaranteed stability and exhibits a larger roll-off at high frequency.

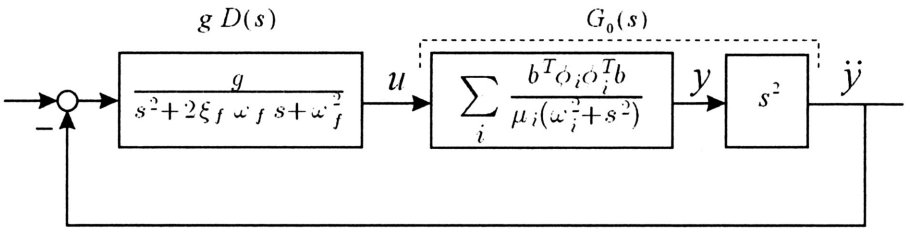

FIGURE 18. Acceleration feedback for a SISO collocated system.

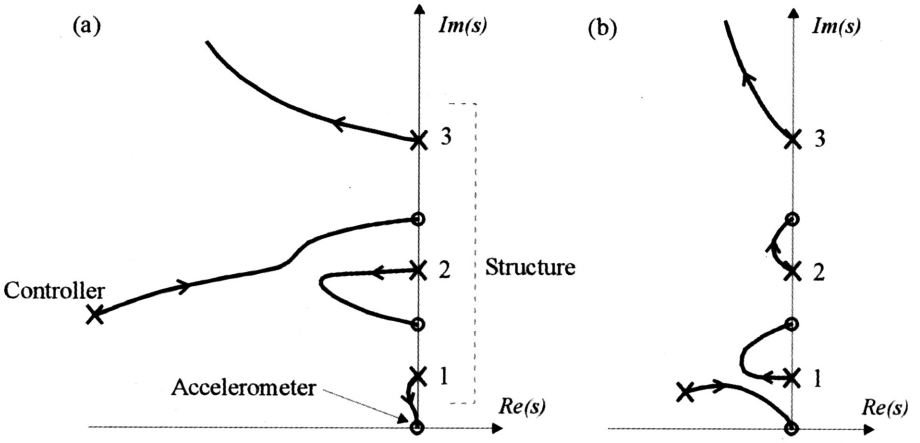

FIGURE 19. Root locus of the acceleration feedback for a m.d.o.f. structure. (a) The control is targeted at mode 2. (b) The control is targeted at mode 1. (Different scales are used for the real and imaginary parts)

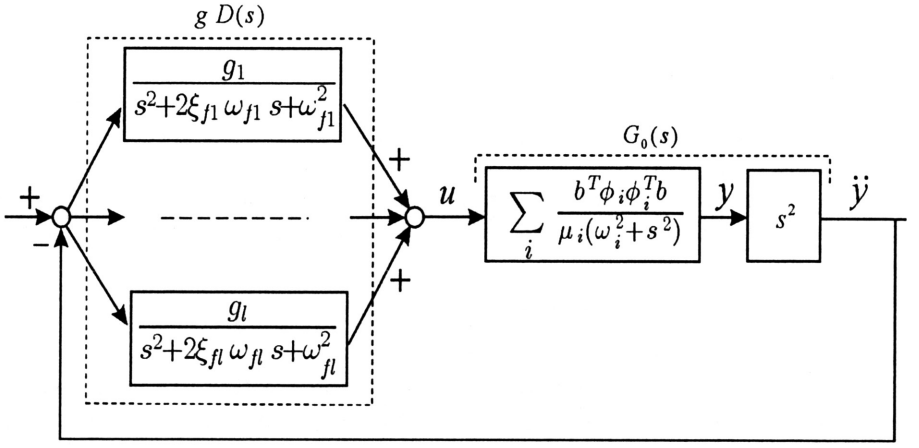

FIGURE 20. Targeting several modes with a SISO acceleration feedback.

7.3.1. Second order filter. The block diagram of the second order filter applied to a SISO collocated system with acceleration sensor is shown in Fig. 18; the corresponding root locus is shown in Fig. 19 for two values of the filter frequency ω_f; in both cases, $\xi_f = 0.5$ is used. In Fig. 19a, ω_f is selected close to the natural frequency of mode 2 while in Fig. 19b, it is selected close to mode 1. Comparing the two figures, we see that all the modes are positively damped, but the mode with the natural frequency close to ω_f is more heavily damped. Thus, the performance of the compensator relies on the tuning of the filter on the mode that we wish to damp (this aspect may become problematic if the system is subject to changes in the parameters). The maximum achievable damping ratio increases with ξ_f; a value of ξ_f between 0.5 and 0.7 is recommended. for closely spaced modes, stability is still guaranteed, but a large damping ratio cannot be achieved simultaneously for the two modes; besides, small variations of the filter frequency may significantly change the root locus and the modal damping.

If several modes must be damped, several compensators may be used in parallel as represented in Fig. 20, where the ω_{fi} are tuned on the targeted modes.

As compared to the Direct Velocity Feedback, $gD(s) = g/s$, the new compensator has a larger roll-off at high frequency (-40 dB/decade instead of -20 dB/decade), which may decrease the risk of destabilizing high frequency modes. The need for tuning the filter frequency ω_f may be a drawback if the natural frequency is not known accurately, or is subject to changes.

7.4. Positive position feedback [14, 10]

The *Positive Position Feedback* (PPF) is appropriate for a structure equipped with strain actuators and sensors; the objective is, once again, to use a second order filter to improve the roll-off of the control system, allowing high frequency gain stabilization. The block diagram is represented in Fig. 21. As compared to Fig. 18, the output y is now proportional to the displacements (e.g. strain sensor) and a minus sign appears in the controller block (together with the minus sign in the feedback loop, this produces a positive feedback.). Figure 22a and b show the root locus when the controller is tuned on mode 1 and mode 2, respectively. We see that the tuning property of the controller is very similar to that of Fig. 18 and, even in presence of a feedthrough component, the open-loop transfer function has a roll-off of -40 dB/decade. However, there is a stability limit which is reached when the open-loop static gain is equal to 1.

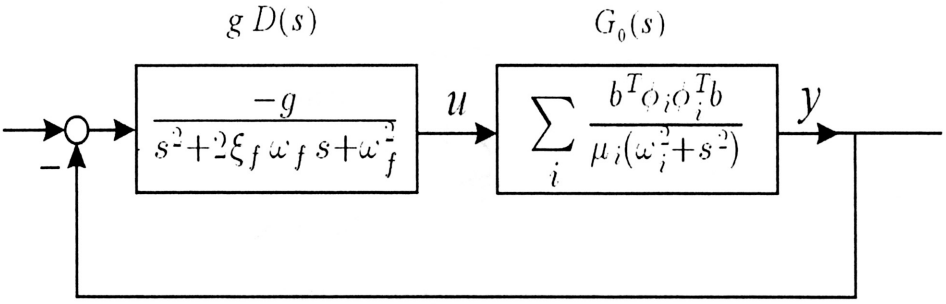

FIGURE 21. Positive Position Feedback for a SISO collocated system.

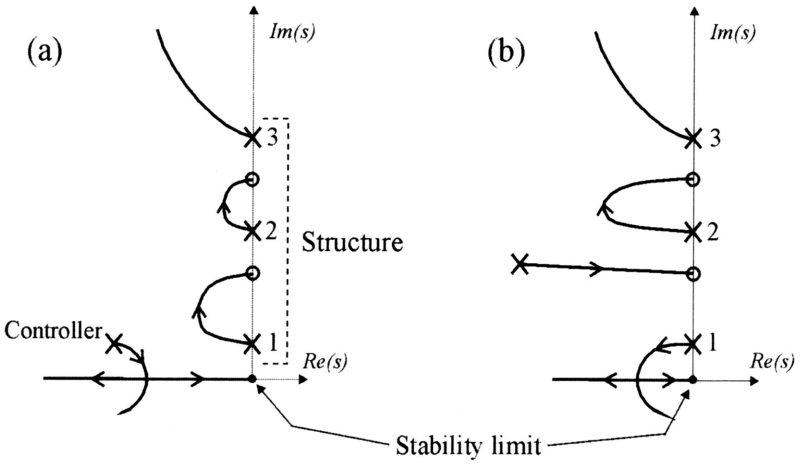

FIGURE 22. Root locus of the PPF. (a) The control is targeted at mode 1. (b) The control is targeted at mode 2.

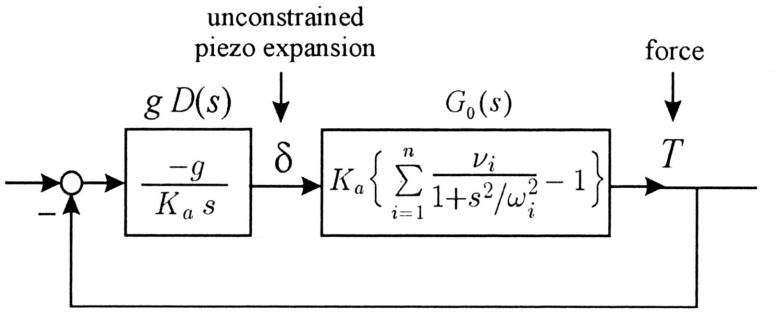

FIGURE 23. Block diagram of the integral force feedback.

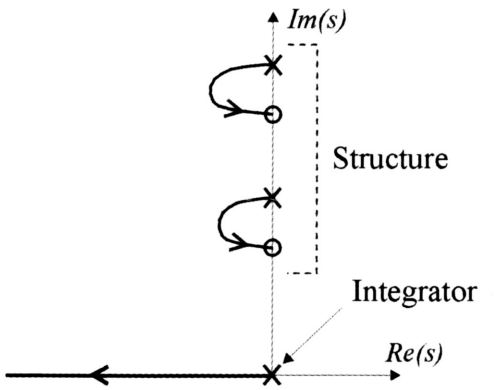

FIGURE 24. Root locus of the integral force feedback.

7.5. Integral force feedback [27]

Consider the active truss of Fig. 14; the open-loop FRF of Eq. (28) has alternating poles and zeros and has no roll-off at high frequencies. This system can be actively damped by a *positive Integral Force Feedback* (Fig. 23); the corresponding root locus is shown in Fig. 24.

7.5.1. Modal damping. Combining the structure equation (24), the sensor equation (26) and the control law

$$\delta = \frac{g}{K_a s} y \tag{36}$$

the closed-loop characteristic equation reads

$$\left[M s^2 + K - \frac{g}{s+g} (b K_a b^T) \right] x = 0. \tag{37}$$

From this equation, we can deduce the open-loop transmission zeros, which coincide with the asymptotic values of the closed-loop poles as $g \to \infty$. Taking the limit, we get

$$\left[M s^2 + (K - b K_a b^T) \right] x = 0, \tag{38}$$

which states that the zeros (i.e. the anti-resonance frequencies) coincide with the poles (resonance frequencies) of the structure where the active strut has been removed (corresponding to the stiffness matrix $K - b K_a b^T$).

To evaluate the modal damping, Eq. (37) must be transformed in modal coordinates with the change of variables $x = \Phi z$. Assuming that the mode shapes have been normalized according to $\Phi^T M \Phi = I$ and taking into account that $\Phi^T K \Phi = \text{diag}(\Omega_i^2) = \Omega^2$, we have

$$\left[I s^2 + \Omega^2 - \frac{g}{s+g} \Phi^T (b K_a b^T) \Phi \right] z = 0. \tag{39}$$

The matrix $\Phi^T (b K_a b^T) \Phi$ is, in general, fully populated; if we assume that it is diagonally dominant, and if we neglect the off-diagonal terms, it can be rewritten

$$\Phi^T (b K_a b^T) \Phi \simeq \text{diag}(\nu_i \Omega_i^2), \tag{40}$$

where ν_i is the *fraction of modal strain energy* in the active member when the structure vibrates according to mode i; ν_i is defined by Eq. (29). Substituting Eq. (40) into (39), we find a set of decoupled equations

$$s^2 + \Omega_i^2 - \frac{g}{s+g} \nu_i \Omega_i^2 = 0 \tag{41}$$

and, after introducing

$$\omega_i^2 = \Omega_i^2 (1 - \nu_i), \tag{42}$$

it can be rewritten

$$s^2 + \Omega_i^2 - \frac{g}{s+g} (\Omega_i^2 - \omega_i^2) = 0. \tag{43}$$

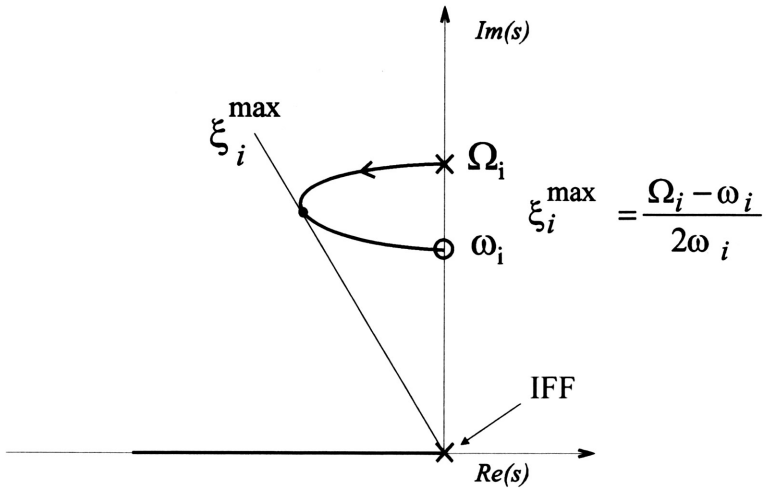

FIGURE 25. Root locus of the closed-loop pole for the IFF.

By comparison with Eq. (37), we see that the transmission zeros (the limit of the closed-loop poles as $g \to \infty$) are $\pm j\omega_i$. The characteristic equation can be rewritten

$$1 + g\frac{(s^2 + \omega_i{}^2)}{s(s^2 + \Omega_i{}^2)} = 0. \tag{44}$$

The corresponding root locus is shown in Fig. 25. The depth of the loop in the left half plane depends on the frequency difference $\Omega_i - \omega_i$, and the maximum modal damping is given by

$$\xi_i{}^{\max} = \frac{\Omega_i - \omega_i}{2\omega_i} \tag{45}$$

it is obtained for $g = \Omega_i\sqrt{\Omega_i/\omega_i}$. For small gains, it can be shown [27] that

$$\xi_i = \frac{g\nu_i}{2\Omega_i}. \tag{46}$$

This interesting result tells us that, for small gains, the active damping ratio in a given mode is proportional to the fraction of modal strain energy in the active element. This result is very useful for the design of active trusses; the active struts should be located in order to maximize the fraction of modal strain energy ν_i in the active members for the critical vibration modes. The preceding results have been established for a single active member; if there are several active members operating with the same control law and the same gain g, this result can be generalized under similar assumptions. It can be shown that each closed-loop pole follows a root locus governed by Eq. (44) where the pole Ω_i is the natural frequency of the open-loop structure and the zero ω_i is the natural frequency of the structure where the active members have been removed.

7.5.2. Experimental results The test structure is shown in Fig. 26. Figures 27 and 28 illustrate typical results. The modal damping ratio of the first two modes is larger than

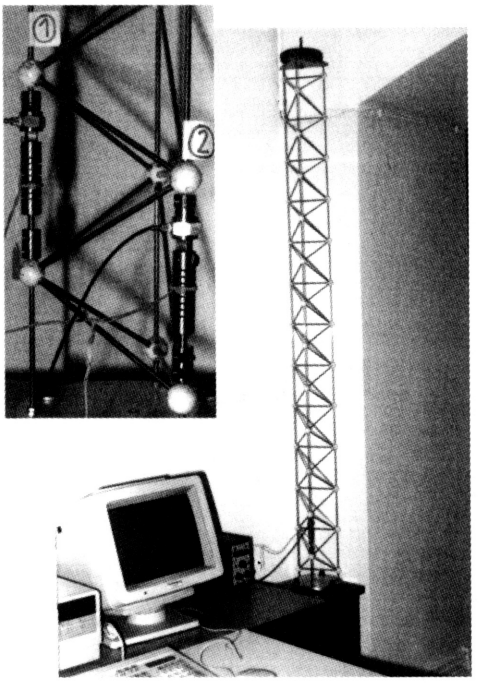

FIGURE 26. Active truss with piezoelectric struts (ULB).

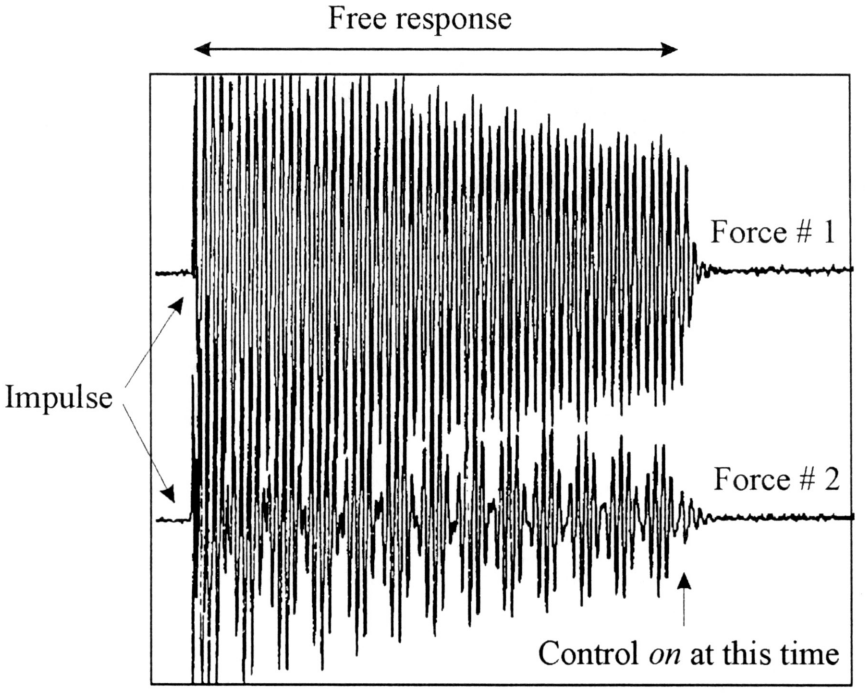

FIGURE 27. Force signal from the two active struts during the free response after impulsive load.

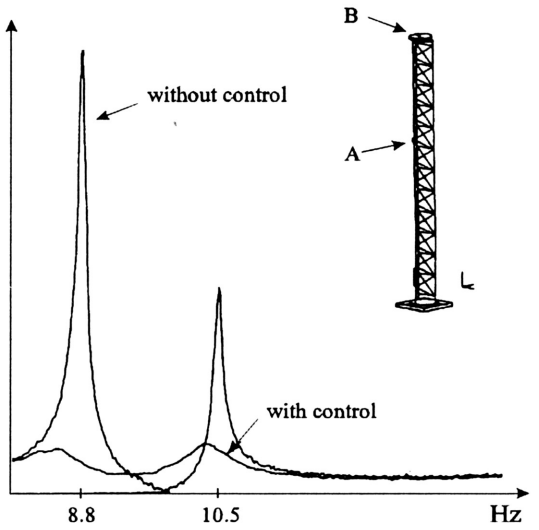

FIGURE 28. FRF between a force in A and an accelerometer in B, with and without control.

10%. Note that, in addition to being simple and robust, the control law can be implemented in a analog controller which performs better in microvibrations.

8. Active tendon control

The use of cables to achieve lightweight structures is not new; it can be found in Herman Oberth's early books on astronautics. The use of guy cables is probably the most efficient way to stiffen a structure, in terms of weight. They can also be used to prestress a deployable structure and eliminate the geometric uncertainty due to the gaps. Cables structures are also extensively used in civil engineering. One further step consists of providing the cables with active tendons to achieve active damping in the structure. This approach has been developed in [23, 1, 2, 24, 25, 26].

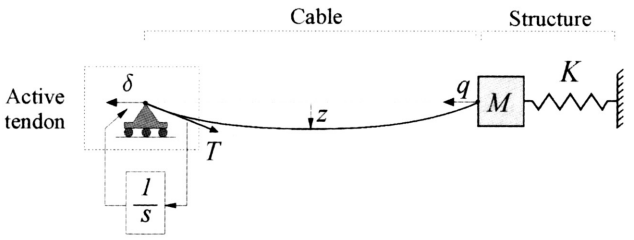

FIGURE 29. Control strategy for active damping of cable structures.

8.1. Active damping of cable structures

When using a displacement actuator (e.g. a piezo) and a force sensor, the (positive) Integral Force Feedback (36) belongs to the class of "energy absorbing" control: indeed, if

$$\delta \sim \int T dt \tag{47}$$

the power flow from the control system is $W = -T\dot{\delta} \sim -T^2 \leq 0$. This means that the control can only extract energy from the system, and this applies to nonlinear structures as well; all the states which are controllable and observable are asymptotically stable for all positive gains (infinite gain margin). The control concept is represented schematically in Fig. 29 where the spring-mass system represents an arbitrary structure. Note that the damping introduced in the cable is usually very low, but experimental results have confirmed that it remains always stable, even at the parametric resonance (when the natural frequency of the structure is twice that of the cables).

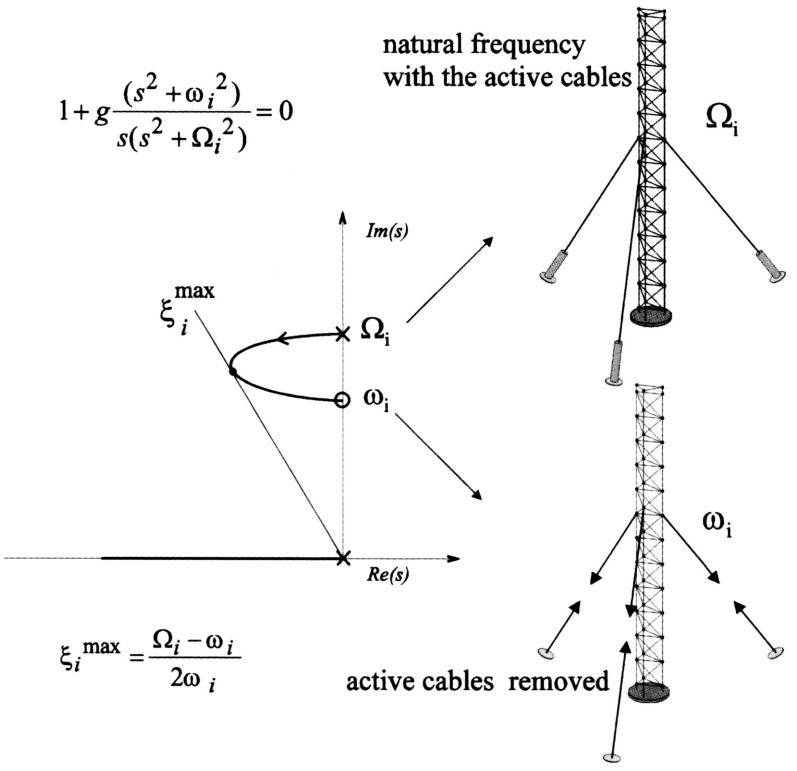

FIGURE 30. Cable structure: root locus of the closed-loop poles.

8.2. Modal damping

If we assume that the dynamics of the cables can be neglected, that their interaction with the structure is restricted to the tension in the cables, and that the global mode shapes are identical with and without the cables, one can develop an approximate linear theory for the closed-loop system; the following results can be established, which follow closely those obtained for active trusses in the foregoing section (we assume no structural damping):

- The open-loop poles are $\pm j\Omega_i$, where Ω_i are the natural frequencies of the structure including the active cables; the open-loop zeros are $\pm j\omega_i$ where ω_i are the natural frequencies of the structure where the active cables have been removed.
- If the same control gain is used for every local control loop, as g goes from 0 to ∞, the closed-loop poles follow the root locus defined by Eq. (44) (Fig. 30). Equation (45) and (46) also apply in this case.

8.3. Active tendon design

Figure 31 shows two possible designs of the active tendon: the first one (bottom left) is based on a linear piezoactuator from PI and a force sensor from B&K; a lever

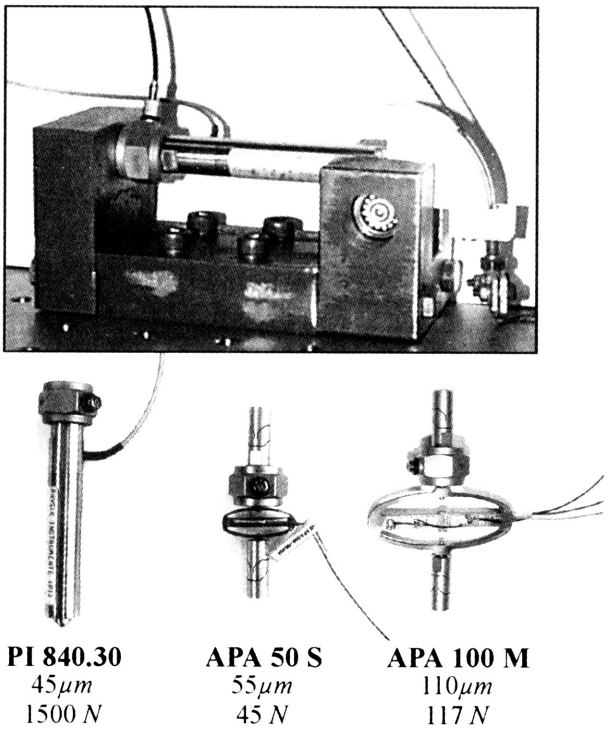

FIGURE 31. Various designs of active tendon or active strut (ULB).

mechanism (top view) is used to transform the tension in the cable into a compression in the piezo stack, and amplifies the translational motion to achieve about 100 μm. This active element is identical to that in an active strut. In the second design (bottom center and right), the linear actuator is replaced by an amplified actuator from CEDRAT Research, also connected to a B&K force sensor and flexible tips. In addition to being more compact, this design does not require an amplification mechanism, and a tension of the flexible tips produces a compression in the piezo stack, which expands in the transverse direction, at the center of the elliptical structure.

8.4. Experimental results

Figure 32 shows the test structure; it is representative of a scale model of the JPL-Micro-Precision-Interferometer [20] which consists of a large trihedral passive truss of about 9 m. The free-floating condition during the test is simulated by hanging the structure from the ceiling of the lab with soft springs. In this study, two different types of cables have been used: a fairly soft cable of 1 mm diameter of polyethylene ($EA \approx 4000$ N) and a stiffer one of synthetic fiber "Dynema" ($EA \approx 18000$ N) ; in both cases, the tension in the cables was chosen in order to set the first cable mode at 400 rad/sec or more, far above the first five flexible modes for which active damping is sought. The table inset into Fig. 32 gives the measured natural frequencies ω_i (without cables) and Ω_i (with cables), for the two sets of cables.

Figure 33 compares the experimental closed-loop poles obtained for increasing gain g of the control with the root locus prediction of Eq. (44). The results are consistent with the analytical predictions, although a larger scatter is observed with stiffer cables. Note, however, that the experimental results tend to exceed the root locus predictions. Figure 34 compares typical FRF with and without control. An analytical study was conducted in [25] to investigate the possibility of using three Kevlar cables of 2 mm diameter connecting the tips of the three trusses of the JPL-MPI. Using the root locus technique of Fig. 30, a damping ratio between 14% and 21% was predicted in the first three flexible modes.

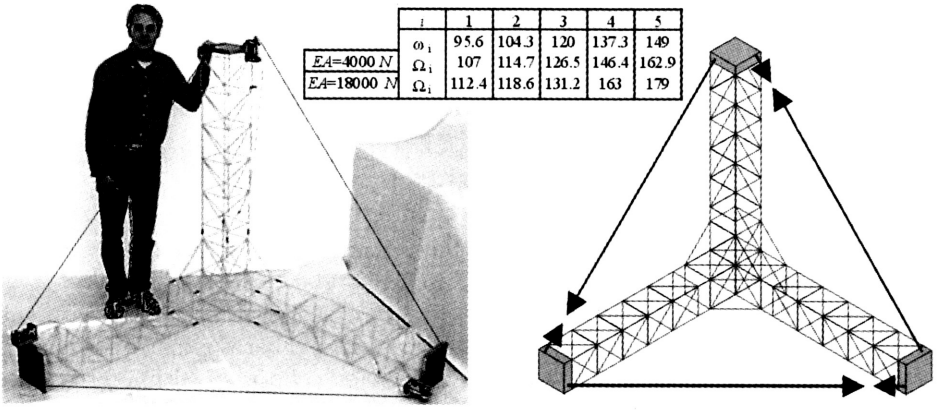

i	1	2	3	4	5
ω_i	95.6	104.3	120	137.3	149
Ω_i (EA=4000 N)	107	114.7	126.5	146.4	162.9
Ω_i (EA=18000 N)	112.4	118.6	131.2	163	179

FIGURE 32. Free floating truss with active tendons.

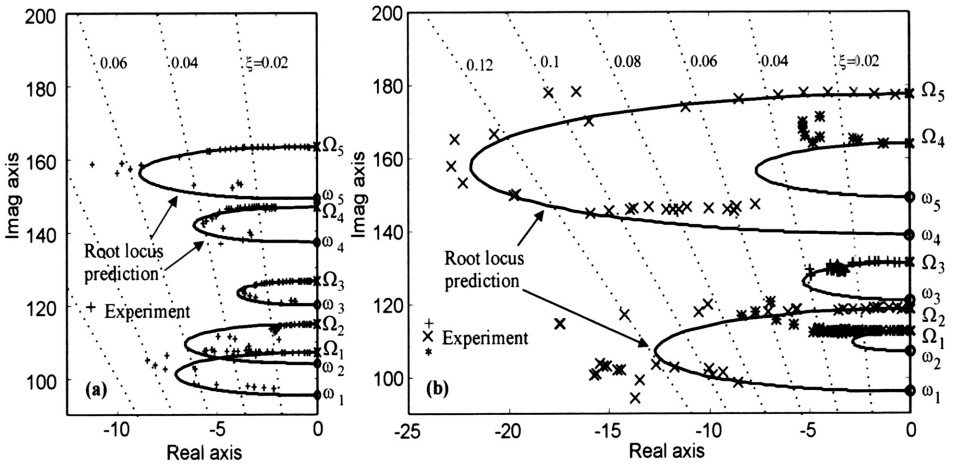

FIGURE 33. Experimental poles vs. root-locus prediction for the flexible modes of the free floating truss. (a) $EA = 4000$ N. (b) $EA = 18000$ N.

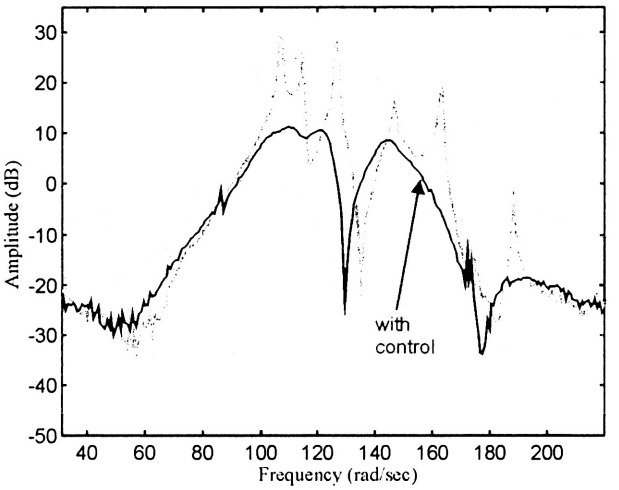

FIGURE 34. Typical FRF with and without control ($EA = 4000$ N).

9. Active damping generic interface

The active strut discussed in Sec. 6 can be developed into a generic 6 d.o.f. interface which can be used to connect arbitrary substructures.

Such an interface is shown in Fig. 35; it consists of a Stewart platform with cubic architecture [13]. Each leg consists of an active strut similar to that shown at the center of Fig. 31: piezotranslator of the amplified design collocated with a force sensor, and connected to the base plates by flexible tips acting like spherical joints. The cubic architecture provides a uniform control capability in all directions, a uniform stiffness in all directions, and minimizes the cross-coupling amongst actuators (which are mutually

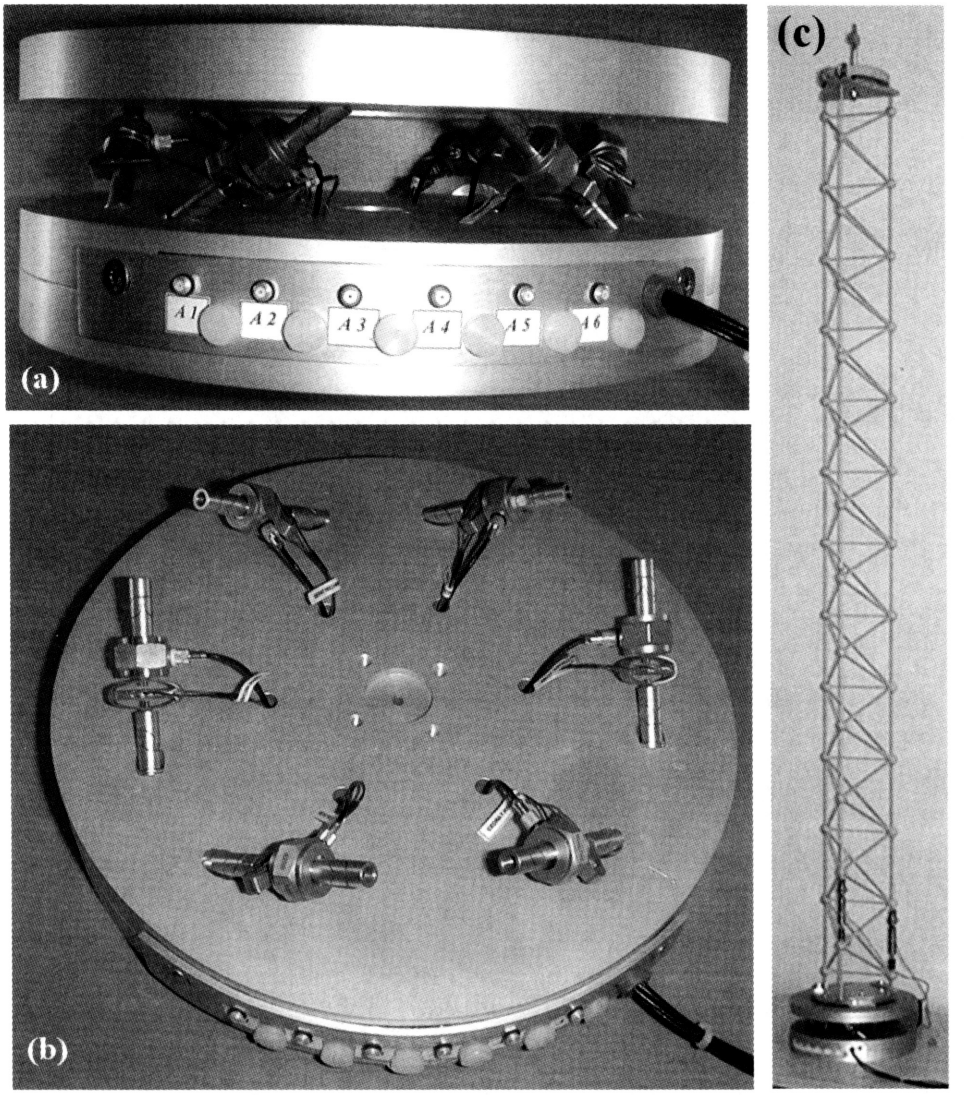

FIGURE 35. Stewart platform with piezoelectric legs as generic active damping interface. (a) General view. (b) With the upper base plate removed. (c) Interface acting as a support of a truss.

orthogonal). The control is decentralized with the same gain for all loops. Figure 35c shows the generic interface mounted between a truss and the supporting structure. Figure 36 shows the evolution of the first two closed-loop poles of this system when we increase the gain of the decentralized controller; the continuous line shows the root locus prediction of Eq. (44); Ω_i are the open-loop natural frequencies while ω_i are the high-gain asymptotes of the closed-loop poles.

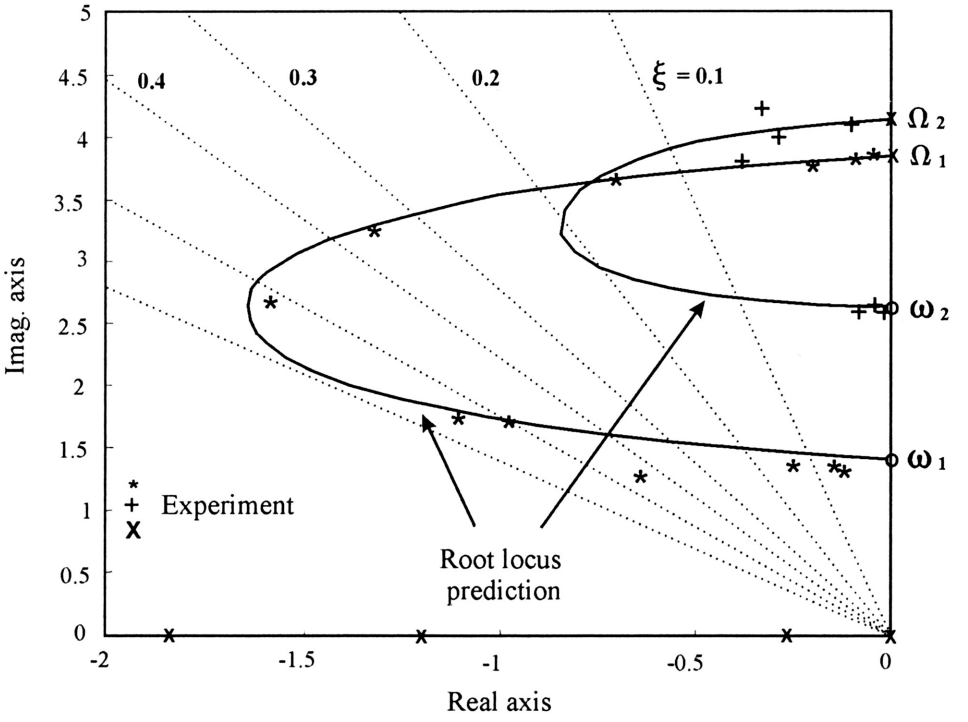

FIGURE 36. Experimental poles and root locus prediction from Eq. (44) for the structure of Fig. 35c.

10. Active vibration isolation

Many operating equipments (e.g. a car engine or an attitude control reaction wheel assembly in a spacecraft) generate oscillatory forces which can propagate in the supporting structure. Conversely, sensitive equipments may be supported by a structure which vibrates appreciably (e.g. a telescope in a spacecraft). In both cases, a vibration isolation is necessary and it turns out that the two problems have the same solution.

10.1. Passive isolation

Let us consider the dirty body/clean body isolation problem (Fig. 37), where the dirty body motion x_d constitutes the disturbance and the clean body displacement x_c is the system output; the passive isolation system consists of a spring and damper. The transmissibility of the isolation system is defined as

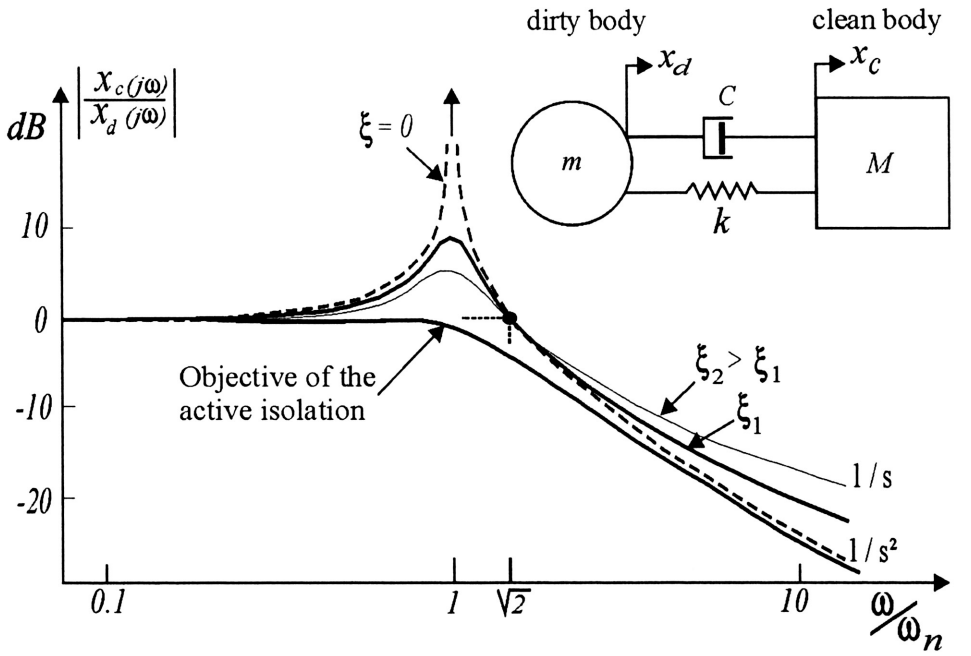

FIGURE 37. Passive isolator transmissibility FRF for various values of the damping ξ.

$$\frac{X_c(s)}{X_d(s)} = \frac{1 + 2\xi s/\omega_n}{1 + 2\xi s/\omega_n + s^2/\omega_n^2}. \tag{48}$$

The amplitude diagram is represented in Fig. 37 for various values of the damping ratio. We observe that

- All the curves are larger than 1 for $\omega < \sqrt{2}\,\omega_n$ and become smaller than 1 for $\omega > \sqrt{2}\,\omega_n$. Thus the critical frequency $\sqrt{2}\omega_n$ separates the domains of amplification and attenuation of the isolator.
- When $\xi = 0$, the high frequency decay rate is $1/s^2$, that is $-40\,\mathrm{dB/decade}$, while very large amplitudes occur near the corner frequency ω_n (the natural frequency of the spring-mass system).
- The damping reduces the amplitude at resonance, but also tends to reduce the effectiveness at high frequency; the high frequency decay rate becomes $1/s$ ($-20\,\mathrm{dB/decade}$).

The design of a passive isolator involves a trade-off between the resonance amplification and the high frequency attenuation; the ideal isolator should have a frequency dependent damping, with high damping below the critical frequency $\sqrt{2}\,\omega_n$ to reduce the amplification peak, and low damping above $\sqrt{2}\,\omega_n$ to improve the decay rate. The objective in designing an active isolation system is to achieve no amplification below ω_n and a decay rate of -40dB/decade at high frequency, as represented in Fig. 37.

10.2. The "sky-hook" damper

Consider the single axis isolator of Fig. 38a; it consists of a soft spring k acting in parallel with a force actuator F_a (note that there is no damping in the isolator). An accelerometer measures the absolute acceleration of the clean body, $\ddot{x}_c$ and an integral controller is used, in such a way that

$$F_a = -gsX_c. \tag{49}$$

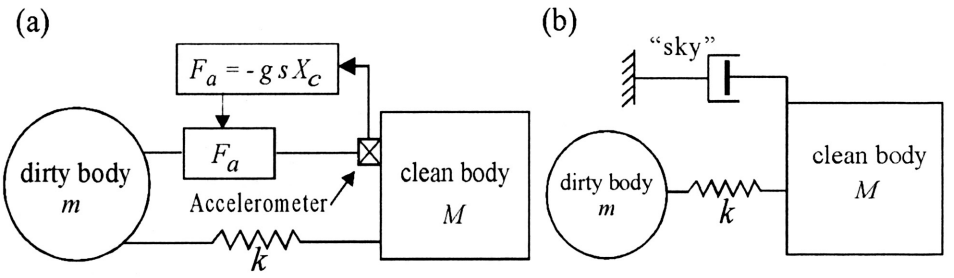

FIGURE 38. (a) Soft isolator with acceleration feedback. (b) Equivalent "sky-hook" damper.

We observe that the resulting control force is proportional to the clean body *absolute* velocity; this is why this control is called "sky-hook damper" (Fig. 38b). It is easy to establish that the closed-loop transmissibility reads

$$\frac{X_c(s)}{X_d(s)} = \left[\frac{M}{k}s^2 + \frac{g}{k}s + 1\right]^{-1}. \tag{50}$$

It has a corner frequency at $\omega_n = \sqrt{k/M}$, its high frequency decay rate is $1/s^2$, that is $-40\,\mathrm{dB/decade}$, and the control gain g can be chosen in such a way that the isolator is critically damped ($\xi = 1$); the corresponding value of the gain is $g = 2\sqrt{kM}$. In this

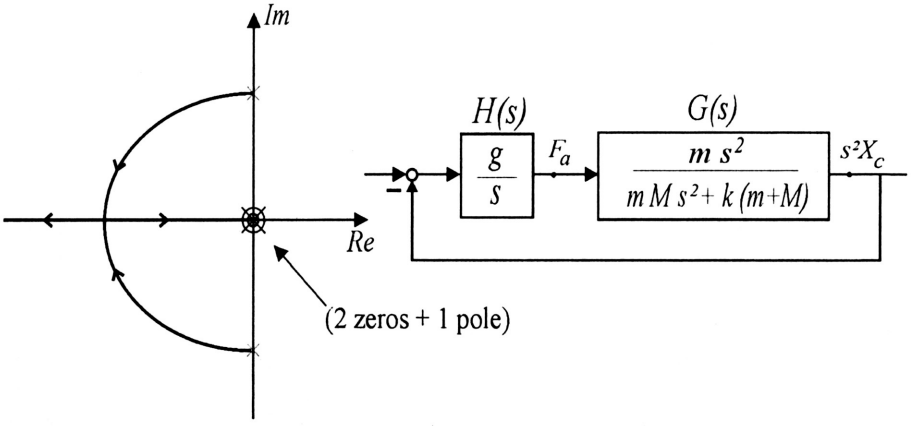

FIGURE 39. Root locus of the sky-hook damper.

way, we achieve a low-pass filter without overshoot with a roll-off of -40dB/decade. This transmissibility follows exactly the objective represented in Fig. 37. On the other hand, the open-loop transfer function of the isolator (between the control force F_a and the clean body acceleration $\ddot{X}_c$) can be written

$$G(s) = \frac{s^2 X_c(s)}{F_a(s)} = \frac{ms^2}{Mms^2 + k(M+m)}. \tag{51}$$

The open-loop poles are the natural frequencies of the system without control. The rigid body modes do not appear in the transfer function (51) because they are not controllable from F_a. The root locus of the closed-loop poles as the gain g of the controller increases is shown in Fig. 39.

10.3. Force feedback

If the clean body is rigid, its acceleration is proportional to the total force transmitted by the interface, $F = F_a + F_k$. As a result, the sky-hook damper can be obtained alternatively with the control configuration of Fig. 40, where a force sensor has been substituted to the acceleration sensor.

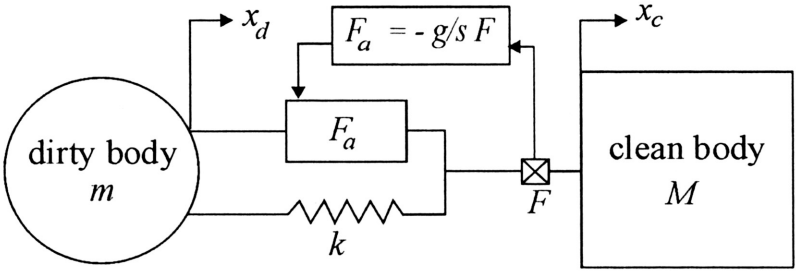

FIGURE 40. Force feedback isolator.

The control strategies based on acceleration feedback and on force feedback appear as totally equivalent for the isolation of rigid bodies. However, the force feedback has two advantages. The first one is related to sensitivity: force sensors with a sensitivity of 10^{-3} N are commonplace and commercially available; if we consider a clean body with a mass of 1000 kg (e.g. a telescope), the corresponding acceleration is 10^{-6} m/s^2. Accelerometers with such a sensitivity are more difficult to find; for example, the most sensitive accelerometer available in the Bruel & Kjaer catalogue is 2.10^{-5} m/s^2 (model 8318). The second advantage is stability when the clean body is flexible. In this case, the sky-hook damper appears to be only conditionally stable (for small gain) when the clean body becomes very flexible, so that the corner frequency of the isolator overlaps with the natural frequencies of the clean body. On the contrary, the stability of the force feedback re mains guaranteed.

10.4. 6 d.o.f. isolator

The foregoing section describes a single axis active isolator which combines a -40 dB/decade attenuation rate in the roll-off region with no overshoot at the cor-

ner frequency. To fully isolate two rigid bodies with respect to each other, we need six such isolators, judiciously placed, that could be controlled either in a centralized or (more likely) in a decentralized manner. For a number of space applications, generic multi-purpose 6 d.o.f. isolators have been developed with a standard *Stewart platform* architecture (Fig. 41) [30, 19]. The Stewart platform uses 6 identical active struts arranged in a mutually orthogonal configuration connecting the corner of a cube (same cubic architecture than in Sec. 9). In addition to the properties discussed in the foregoing section, this cubic architecture also tends to minimize the spread of the modal frequencies of the isolator.

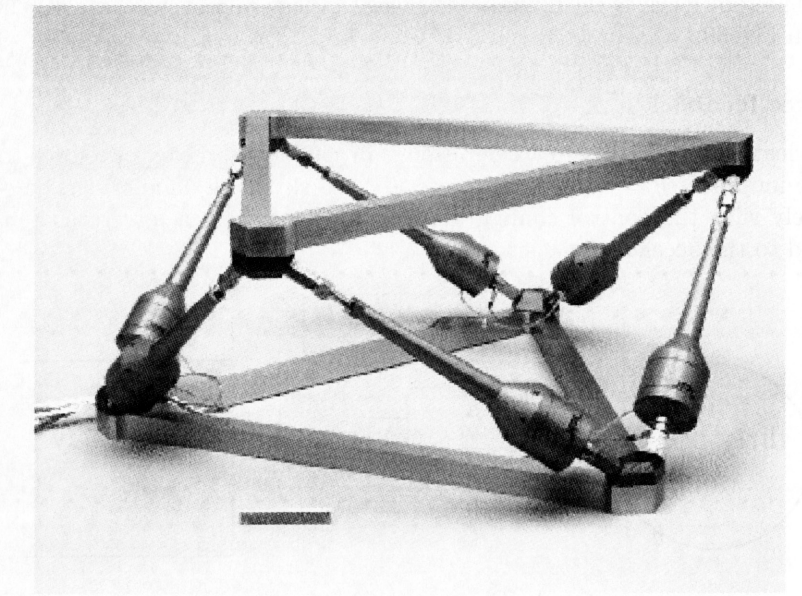

FIGURE 41. Multi-purpose soft isolator based on a Stewart platform (JPL).

10.5. Decentralized control of the 6 d.o.f. isolator

Assuming that the base is fixed and that the payload attached to the upper part of the isolator is a rigid body, the dynamic equation (for small rotations) of the isolator is

$$M\ddot{x} + Kx = Bu, \tag{52}$$

where $x = (x_r, y_r, z_r, \theta_x, \theta_y, \theta_z)^T$ is the vector describing the small displacements and rotations in the payload frame, $u = (u_1, \ldots, u_6)^T$ is the vector of active control forces in strut 1 to 6, and B is their influence matrix in the payload frame. M is the mass matrix and $K = kBB^T$ is the stiffness matrix.

If each leg is equipped with a force sensor as in Fig. 40, the output equation reads

$$y = -kB^T x + u. \tag{53}$$

This equation expresses the fact that the total force is the sum of the spring force and the control force. Once again, we note that the same matrix B appears in Eqs. (52)

and (53) because the sensors and actuators are collocated. Using a decentralized integral force feedback with constant gain, the controller equation reads

$$u = -\frac{g}{s}y. \tag{54}$$

Combining Eqs. (52), (53) and (54), the closed-loop equation reads

$$Ms^2x + Kx = \frac{g}{s+g}kBB^Tx$$

and, taking into account that $K = kBB^T$,

$$\left[Ms^2 + K\frac{s}{s+g}\right]x = 0 \tag{55}$$

If we transform into modal coordinates, $x = \Phi z$, and take into account the orthogonality relationships of the mode shapes, the characteristic equation is reduced to a set of uncoupled equations

$$(s^2 + \Omega_i^2\frac{s}{s+g})z_i = 0 \tag{56}$$

Thus, every mode follows the characteristic equation

$$s^2 + \Omega_i^2\frac{s}{s+g} = 0$$

or

$$1 + g\frac{s}{s^2+\Omega_i^2} = 0. \tag{57}$$

The corresponding root locus is shown in Fig. 42. It is identical to Fig. 39 for a single-axis isolator; however, unless the 6 natural frequencies are identical, a given value of the gain g will lead to different pole locations for the various modes and it will not be possible to achieve the same damping for all modes. This is why it is recommended to locate the payload in such a way that the spread of the modal frequencies is minimized.

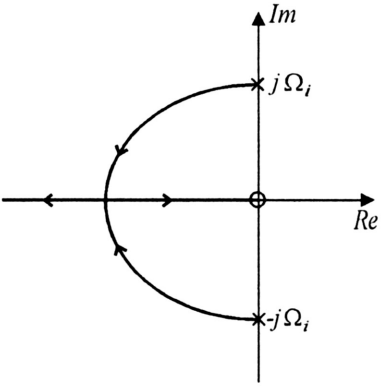

FIGURE 42. Root locus of the modes of the six-axis isolator with integral force feedback.

10.6. Vehicle suspension

Figure 43 shows a quarter-car model of a vehicle. Although this 2 d.o.f. model is too simple for performing a comprehensive analysis of the ride motion, it is sufficient to gain some insight in the behaviour of passive and active suspensions in terms of vibration isolation (represented by the body acceleration $\ddot{x}$), suspension travel $(x - x_0)$ and road holding (represented by the tyre deflexion $x_0 - d$). Typical numerical values used in the simulation reported later are also given in the figure (taken from [7]). The stiffness k_t

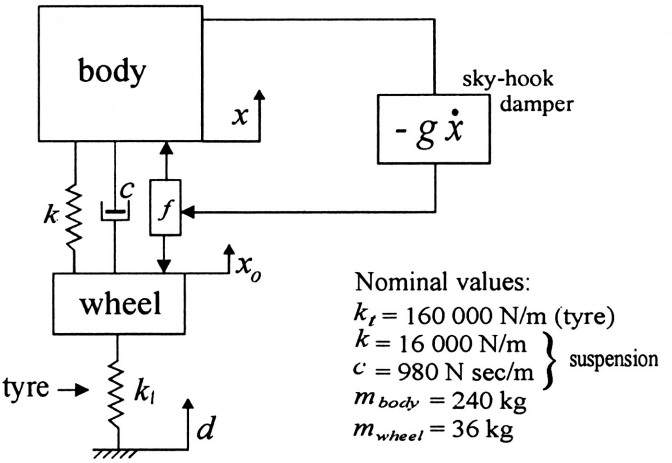

FIGURE 43. *Quarter-car model and sky-hook damper.*

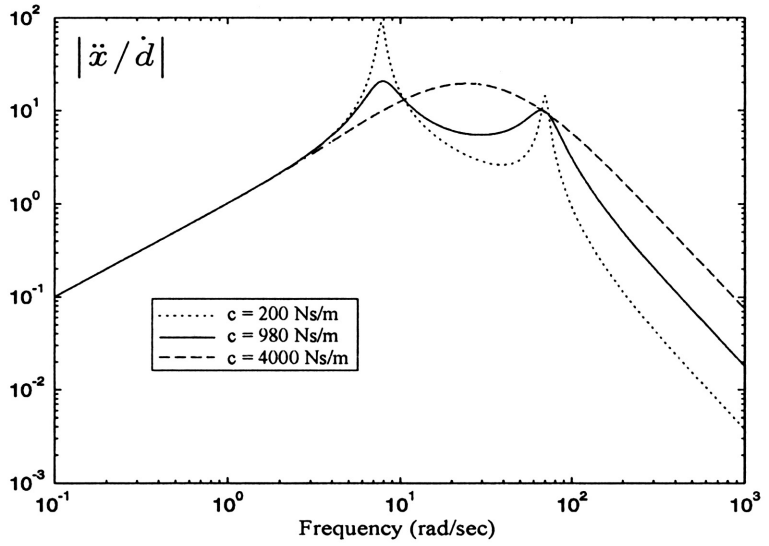

FIGURE 44. FRF of the passive suspension $(\ddot{x}/\dot{d})$ for various values of the damping coefficient.

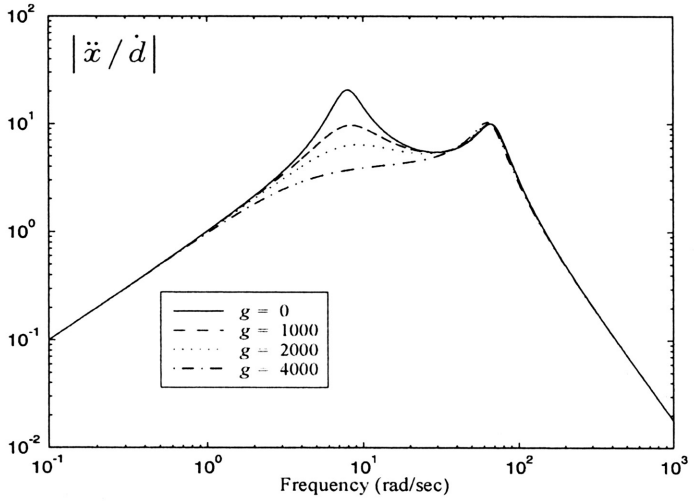

FIGURE 45. FRF of the active suspension ($\ddot{x}/\dot{d}$) for various values of the gain g of the sky-hook damper (all the other parameters have the nominal values listed in Fig. 43).

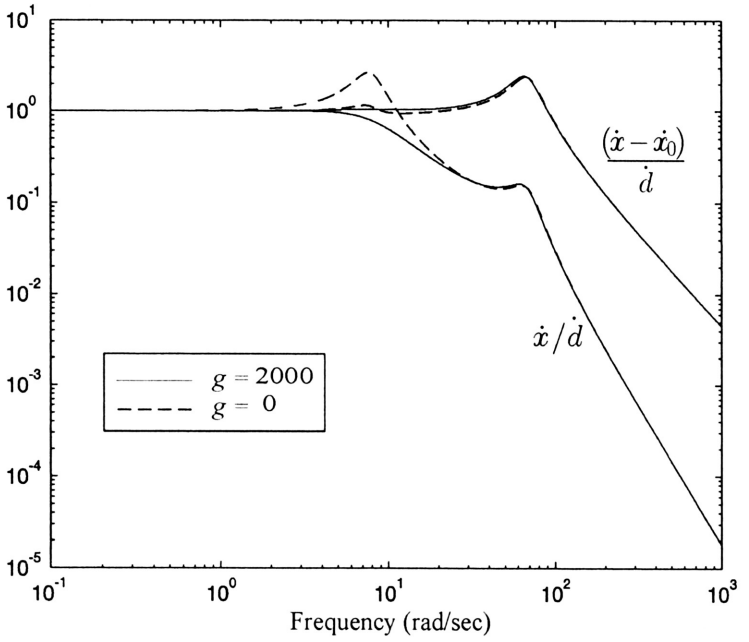

FIGURE 46. Comparison of $|\dot{x}/\dot{d}|$ and $|(\dot{x}-\dot{x}_0)/\dot{d}|$.

corresponds to the tyre; the suspension consists of a passive part (spring k + damper c) and an active one, assumed to be a perfect force actuator acting as a sky-hook damper in this case (the active control force is applied on both sides of the active device, to the body and to the wheel of the vehicle).

Figure 44 shows the *FRF* from the roadway vertical velocity $\dot{d}$ to the car body acceleration $\ddot{x}$ for the passive suspension alone; several values of the damping coefficient c are considered. The first peak corresponds to the body resonance (also called sprung mass resonance) and the second one to the wheel resonance (unsprung mass resonance). The passive damping cannot control the body resonance without reducing the isolation at higher frequency. Next, a sky-hook damper ($f = -g\dot{x}$) is added. Figure 45 shows the corresponding *FRF* from $\dot{d}$ to $\ddot{x}$ for various values of the control gain. Note that the body resonance can be damped without reducing the isolation at higher frequency but the peak in the *FRF* corresponding to the wheel resonance cannot be changed by the active control. Figure 46 compares the amplitude of the *FRF* $\dot{x}/\dot{d}$ and $(\dot{x} - \dot{x}_0)/\dot{d}$ for two values of the gain. This figure shows that the absolute velocity of the body $\dot{x}$ rolls-off much faster (i.e. has much lower fr equency components) than the relative velocity $(\dot{x} - \dot{x}_0)$. This point is important in the design of semi-active suspension devices which try to emulate the sky-hook damper by acting on the flow parameters of the damper acting on the *relative* velocity.

References

1. Y. ACHKIRE, *Active Tendon Control of Cable-Stayed Bridges*, Ph.D. thesis, Active Structures Laboratory, Université Libre de Bruxelles, Belgium 1997.
2. Y. ACHKIRE and A. PREUMONT, *Active Tendon Control of Cable-Stayed Bridges*, Earthquake Engineering and Structural Dynamics, Vol.25(6), 585–597, 1996.
3. B.D. AGARWAL and L.J. BROUTMAN, *Analysis and Performance of Fiber Composites*, Wiley, second edn., 1990.
4. E.H. ANDERSON, D.M. MOORE, J.L. FANSON and M.A. EALEY, *Development of an Active Member Using Piezoelectric and Electrostrictive Actuation for Control of Precision Structures*, SDM Conference, AIAA paper 90-1085-CP, 1990.
5. J.N. AUBRUN, *Theory of the Control of Structures by Low-Authority Controllers*, AIAA J. of Guidance, Vol.3(5), 444–451, 1980.
6. M.J. BALAS, *Direct Velocity Feedback Control of Large Space Structures*, AIAA J. of Guidance, Vol.2(3), 252–253, 1979.
7. R.M. CHALASANI, *Ride Performance Potential of Active Suspension Systems, Part1: Simplified Analysis Based on a Quarter-Car Model*, ASME Symposium on Simulation and Control of Ground vehicles and Transportation systems, Anaheim, CA, 1984.
8. G. CHEN, B. LURIE and B. WADA, *Experimental Studies of Adaptive Structure for Precision Performance*, Proceedings of the 30th AIAA/ASME/ASCE/AHS Structures, Structural Dynamics, and Materials Conference, AIAA, Washington DC, pp.1462–1472, 1989.
9. J.L. FANSON, G.H. BLACKWOOD and C.C. CHEN, *Active Member Control of Precision Structures*, SDM Conference, AIAA paper 89-1329-CP, 1989.
10. J.L. FANSON and T.K. CAUGHEY, *Positive Position Feedback Control for Large Space Structures*, AIAA Journal, Vol.28(4), 717–724, 1990.
11. R.L. FORWARD, *Electronic Damping of Orthogonal Bending Modes in a Cylindrical Mast Experiment*, AIAA Journal of Spacecraft, Vol.18(1), 11–17, 1981.

12. C.R. FULLER, S.J. ELLIOTT and P.A. NELSON, *Active Control of Vibration*, Academic Press, 1996.

13. Z.J. GENG and L.S. HAYNES, *Six Degree-of-Freedom Active Vibration Control Using the Stewart Platforms*, IEEE Transactions on Control Systems Technology, Vol.2(1), 45–53, 1994.

14. C. GOH and T.K. CAUGHEY, *On the Stability Problem Caused by Finite Actuator Dynamics in the Control of Large Space Structures*, Int. J. of Control, Vol.41(3), 787–802, 1985.

15. C.E. KAPLOW and J.R. VELMAN, *Active Local Vibration Isolation Applied to a Flexible Space Telescope*, AIAA J. Guidance and Control, Vol.3(3), 227–233, 1980.

16. D.C. KARNOPP and A.K. TRIKHA, *Comparative Study of Optimization Techniques for Shock and Vibration Isolation*, Trans. ASME, Journal of Engineering for Industry, series B, Vol.91(4), 1128–1132, 1969.

17. C.-K. LEE, *Theory of Laminated Piezoelectric Plates for the Design of Distributed Sensors/Actuators – Part I: Governing Equations and Reciprocal Relationships*, J. Acoust.-Soc. Am, Vol.87(3), 1144–1158, 1990.

18. C.-K. LEE and F.C. MOON, *Modal Sensors/Actuators* Trans. ASME, J. of Applied Mechanics, Vol.57, 434–441, 1990.

19. J.E. MCINROY, G.W. NEAT and J.F. O'BRIEN, *A Robotic Approach to Fault-Tolerant, Precision Pointing*, IEEE Robotics & Automation Magazine, pp.24–31, 1999.

20. G. NEAT, A. ABRAMOVICI, J. MELODY, R. CALVET, N. NERHEIM and J. O'BRIEN, *Control Technology Readiness for Spaceborne Optical Interferometer Missions*, Proceedings SMACS-2, Toulouse, pp.13–32, 1997.

21. P.A. NELSON and S.J. ELLIOTT, *Active Control of Sound*, Academic Press, 1992.

22. V. PIEFORT, *Finite Element Modeling of Piezoelectric Active Structures*, Ph.D. thesis, Université Libre de Bruxelles, Active Structures Laboratory, 2001.

23. A. PREUMONT, *Vibration Control of Active Structures, an Introduction*, Kluwer Academic Publishers, 1997.

24. A. PREUMONT and Y. ACHKIRE, *Active Damping of Structures with Guy Cables*, AIAA, J. of Guidance, Control, and Dynamics, Vol.20(2), 320–326, 1997.

25. A. PREUMONT, Y. ACHKIRE and F. BOSSENS, *Active Tendon Control of Large Trusses*, AIAA Journal, Vol.38(3), 493–498, 2000.

26. A. PREUMONT and F. BOSSENS, *Active Tendon Control of Vibration of Truss Structures: Theory and Experiments*, Journal of Intelligent Material Systems and Structures, Vol.11(2), 91–99, 2000.

27. A. PREUMONT, J.P. DUFOUR and C. MALEKIAN, *Active Damping by a Local Force Feedback with Piezoelectric Actuators*, AIAA J. of Guidance, Vol.15(2), 390–395, 1992.

28. A. PREUMONT, N. LOIX, D. MALAISE and O. LECRENIER, *Active Damping of Optical Test Benches with Acceleration Feedback*, Machine Vibration, Vol.2, 119–124, 1993.

29. E. SIM and S.W. LEE, *Active Vibration Control of Flexible Structures with Acceleration or Combined Feedback*, AIAA J. of Guidance, Vol.16(2), 413–415, 1993.

30. J. SPANOS, Z. RAHMAN and G. BLACKWOOD, *A Soft 6-Axis Active Vibration Isolator*, Proceedings of the American Control Conference, Seattle, WA, pp.412–416, 1995.

31. D. THAYER, J. VAGNERS, A. VON FLOTOW, C. HARDHAM and K. SCRIBNER, *Six-Axis Vibration Isolation System Using Soft Actuators and Multiple Sensors*, Proc. of Annual American Astronautical Society Rocky Mountain Guidance and Control Conference (AAS-98-064), pp.497–506, 1998.